SYNTHESIZING GERMANIUM AND SILICON NANOCRYSTALS EMBEDDED IN SILICON DIOXIDE BY MAGNETRON SPUTTERING DEPOSITION TECHNIQUE

A THESIS SUBMITTED TO
THE GRADUATE SCHOOL OF NATURAL AND APPLIED SCIENCES
OF
MIDDLE EAST TECHNICAL UNIVERSITY

BY

ARİF SİNAN ALAGÖZ

IN PARTIAL FULFILLMENT OF THE REQUIREMENTS
FOR
THE DEGREE OF MASTER OF SCIENCE
IN
PHYSICS

JULY 2007

Approval of Thesis

SYNTHESIZING GERMANIUM AND SILICON NANOCRYSTALS EMBEDDED IN SILICON DIOXIDE BY MAGNETRON SPUTTERING DEPOSITION TECHNIQUE

Submitted by Arif Sinan ALAGÖZ in partial fulfillment of the requirements for the degree of master of science in physics by,

Prof. Dr. Canan ÖZGEN
Dean, Graduate School of Natural and Applied Sciences _________________

Prof. Dr. Sinan BİLİKMEN
Head of Department, Physics, METU _________________

Prof. Dr. Raşit TURAN
Supervisor, Physics, METU _________________

Examining Committee Members

Prof. Dr. Çiğdem ERÇELEBİ
Physics, METU _________________

Prof. Dr. Raşit TURAN
Supervisor, Physics, METU _________________

Prof. Dr. Nizami HASANLI
Physics, METU _________________

Prof. Dr. Mehmet PARLAK
Physics, METU _________________

Dr. Baybars ORAL
VAKSİS R&D LTD. _________________

Date: _________________

I hereby declare that all information in this document has been obtained and presented in accordance with academic rules and ethical conduct. I also declare that, as required by these rules and conduct, I have fully cited and referenced all material and results that are not original to this work.

Name SURNAME: Arif Sinan ALAGÖZ

Signature :

ABSTRACT

SYNTHESIZING GERMANIUM AND SILICON NANOCRYSTALS EMBEDDED IN SILICON DIOXIDE BY MAGNETRON SPUTTERING DEPOSITION TECHNIQUE

Alagöz, Arif Sinan
M.Sc., Department of Physics
Supervisor: Prof. Dr. Raşit TURAN

July 2007, 72 pages

Applications of semiconductor nanocrystal in electronics are promising. Various techniques were developed to synthesize and analyze semiconductor nanocrystals for integrated circuit applications. In this study, silicon and germanium nanocrystals were synthesized in silicon dioxide matrix by magnetron sputtering deposition and following high temperature furnace annealing. Multilayer and single layer samples were prepared by co-sputtering depositions. Transmission electron microscopy measurements were carried out to analyze annealing effects on nanocrystal size distribution, change in shape, density and localization in silicon dioxide (SiO_2). Ge-Ge Traverse Optical (TO) peak was monitored using Raman spectroscopy to investigate germanium nanocrystal formation and stress effects of silicon dioxide. Si-O-Si asymmetric stretching band is examined by Fourier transform infrared transmission spectroscopy to study silicon dioxide matrix recovery with germanium nanocrystal formation. Luminescence characteristics of silicon nanocrystals in visible and near infrared region (550nm-1050nm) with changing nanocrystal size and density were studied with photoluminescence spectroscopy.

Keywords: Magnetron sputtering, silicon, germanium, nanocrystal, silicon dioxide

ÖZ

MAGNETRON SAÇTIRMA TEKNİĞİ İLE SİLİSYUM DİOKSİT İÇERİSİNDE SİLİSYUM VE GERMANYUM NANOKRİSTALLERİN SENTEZLEMESİ

Alagöz, Arif Sinan
Yüksek Lisans, Fizik Bölümü
Tez Yöneticisi: Prof. Dr. Raşit Turan

Temmuz 2007, 72 sayfa

Yar›iletken nanokristallerin elektronikteki uygulamalar› gelecek vadeden alanlar aras›nda yer almaktad›r. Entegre devre uygulamalar›nda kullan›lmak üzere yar›-iletken nanokristallerin sentezlenmesi ve analiz edilmesi için birçok teknik geliştirilmiştir. Bu çalışmada, silisyum ve germanyum nano-kristallerin silisyum dioksit içerisinde mıknatıslı saçtırma yöntemi ve peşi sıra yüksek sıcaklıkta fırınlanmayla sentezlenmiştir. Tek katmanlı ve çok katmanlı örnekler eş-saçt›rma yöntemiyle hazırlanmışlardır. Yoğunluk ve fırınlama koşullar›n›n nano-kristallerin büyüklük dağılımı, şekilleri, yoğunluğu ve oluşturuldukları matris yapı içerisindeki konumlanmaları üzerindeki etkileri elektron mikroskopisi ölçümleri ile incelenmiştir. Ge-Ge TO tepesi Raman spektroskopisi ile incelenerek germanyum nano-kristaller oluşumu ve üzerlerinde oluşan oksit stresinin izlenmiştir. Si-O-Si asimetrik gerilim bandı Fourier dönüşümlü kızıl ötesi spektroskopisi ile incelenerek silisyum dioksit yap›n›n germanyum nano-kristal oluşumuyla iyileşmesi üzerine çalışılmıştır.

Silisyum nano-kristallerin boyutlarındaki ve yoğunluklarındaki değişimle görünür ve yak›n k›z›l-ötesi bölgede (550nm-1050nm) ışıma özellikleri fotolüminesans spektroskopisi ile çalışılmıştır.

Anahtar Kelimeler: M›knat›sl› saçt›rma, silisyum, germanyum, nanokristal, silisyum dioksit

to my lovely family…

ACKNOWLEDGEMENTS

I faithfully thank to my supervisor Prof. Dr. Raşit Turan for guidance through my master work. Also I would like to thank to Prof. Dr. Çiğdem Erçelebi, Prof. Dr. Mehmet Parlak, Prof. Dr. Nizami Hasanlı and Dr. Baybars Oral for their valuable criticism to my thesis.

I want to acknowledge Umut Bostancı, Mustafa Kulakçı, Arife Imer, Ayşe Seyhan, Nader Asghar, Mustafa Fatih Genişel, Aykutlu Dane, Terge G. Finstad, Mehmet Emre Kabadayı and Yücel Eke for both friendships and helps in my experimental works.

I want to thank specially to my officemate Kadir Gökşen who was like a big brother for me.

It is impossible for me to express my gratitude to my family nevertheless I want to thank them for everything.

TABLE OF CONTENTS

ABSTRACT ……………………………………………………………………... iv
ÖZ ……………………………………………………………………………... vi
DEDICATION …………………………………………………………….... viii
ACKNOWLEDGMENTS ……………………………………………….. ix
TABLE OF CONTENTS ……………………………………………….... x
LIST OF TABLES ……………………………………………………… xiii
LIST OF FIGURES ……………………………………………………… xiv
CHAPTERS ……………………………………………………………...
1. INTRODUCTION ………………………………………………… 1
    1.1. Motivation …………………………………………………. 1
        1.1.1. FLASH Memory Application of Germanium Nanocrystal 2
        1.1.2. Light Emitting Diode Application of Silicon Nanocrystals 4
    1.2. Fabrication of Silicon and Germanium Nanocrystals Embedded in Silicon Dioxide ……..………………………………………… 5
        1.2.1. Ostwald Ripening ……………………………………... 5
        1.2.2. Ion Implantation Technique ……………………………... 7
        1.2.3. Chemical Vapor Deposition Technique …………………. 8
        1.2.4. Laser Ablation Deposition Technique …………………… 9
        1.2.5. Magnetron Sputtering Deposition Technique …………… 10
2. MAGNETRON SPUTTERING DEPOSITION TECHNIQUE …….. 11
    2.1. Sputtering and Its Applications …………………………………. 11
    2.2. Sputtering Parameters ……………………………………….... 14
        2.2.1. Sputtering Yield ………………………………………. 14
        2.2.2. Target Material ……………………………………….... 14
        2.2.3. Crystal Structure of Target ………………………………. 15
        2.2.4. Sputtering Gas ………………………………………… 17
        2.2.5. Projectile Energy ……………………………………… 19

2.2.6. Incidence Angle of Projectile ………………………………. 21
2.2.7. Sputtering Rate ………………………………………….... 22
2.3. Film Deposition ………………………………………………. 22
2.3.1. Gas Pressure and Power …………………………………. 22
2.3.2. Deposition Geometry…………………………………….... 23
2.3.3. Condensation Efficiency ………………………………… 27
2.3.4. Substrate Heating ………………………………………… 27
2.4. Experimental Method and Setup ………………………….... 28
2.4.1. DC & RF Sputtering …………………………………….... 28
2.4.2. Magnetron Sputtering ……………………………………. 29
2.4.3. nano-D 100 ………………………………………………. 29
3. SYNTHESIS AND CHARACTERIZATION OF GERMANIUM NANOCRYSTALS …………………………………………….. 31
3.1. Sample Preparation …………………………………………... 31
3.2. Transmission Electron Microscopy …………………………... 33
3.2.1. Instrumentation …………………………………………... 33
3.2.2. Measurements and Discussion …………………………... 33
3.3. Raman Spectroscopy …………………………………………. 39
3.3.1. Instrumentation …………………………………………... 39
3.3.2. Measurements and Discussion …………………………... 39
3.4. Fourier Transform Infrared Spectroscopy ……………………. 42
3.4.1. Instrumentation …………………………………………... 42
3.4.2. Measurements and Discussion 43
4. SYNTHESIS AND CHARACTERIZATION OF SILICON NANOCRYSTALS …………………………………………….. 48
4.1. Sample Preparation …………………………………………... 48
4.2. Transmission Electron Microscopy …………………………... 51
4.2.1. Instrumentation ………………………………………….. 51
4.2.2. Measurements and Discussion …………………………... 51
4.2.2.1. Set 1 ………………………………………………… 51
4.2.2.2. Set 2 ………………………………………………… 53
4.3. Photoluminescence Spectroscopy ……………………………. 58
4.3.1. Instrumentation …………………………………………... 58

4.3.2. Measurements and Discussion ………………………….. 58
5. CONCLUSION ……………………………………………………… 65
REFERENCES …………………………………………………………….. 67

LIST OF TABLES

TABLES

Table 2.1 Sputtering threshold (eV) and heat of sublimation (eV) data of various elemental targets for different projectiles …………………. 20

Table 2.2 Sputtering rate for various targets at 1.0mA/cm^2 Ar$^+$ current density and 500V acceleration voltage …………………………………….. 22

Table 3.1 Sputtering conditions of multilayer and single layer samples …….. 33

Table 4.1 Sputtering conditions of multilayer sample S1 ………………....... 53

Table 4.2 Sputtering conditions of multilayer sample S2 and two layer Si-L series ……………………………………………………………….. 53

LIST OF FIGURES

FIGURES

Figure 1.1 Microelectronics technology evolution timeline 1
Figure 1.2 Intel microprocessor evolution timeline 2
Figure 1.3 Schematic diagram of conventional floating gate FLASH memory cell 3
Figure 1.4 Schematic diagram of nanocrystal based FLASH memory cell .. 4
Figure 1.5 Schematic diagram of Si nanocrystal embedded MOS-LED 5
Figure 1.6 Plot of atom loss from an individual particle 6
Figure 1.7 Schematic diagram of an ion implanter system 8
Figure 1.8 Schematic diagram of a plasma enhanced chemical vapor deposition system 9
Figure 1.9 Schematic diagram of a laser ablation deposition system 10
Figure 2.1 Schematic diagrams of cascaded collusions and sputtering process 12
Figure 2.2 Schematic diagram of a sputtering deposition system 13
Figure 2.3 Sputtering yields of several elemental targets at 1 keV Ar$^+$ bombardment 14
Figure 2.4 Inverse sublimation energy of several elemental targets 15
Figure 2.5 Crystal structure dependence of sputtering yield 16
Figure 2.6 Channeling effect on sputtering yield of Cu (111) target and comparison with polycrystalline Cu target with bombardment of 27 keV Ar$^+$ 16
Figure 2.7 Theoretical and empirical sputtering yields of column IV B elements for different noble sputtering gases 17
Figure 2.8 Variation in sputtering yield with sputtering gas 18
Figure 2.9 Threshold energy and energy dependence of sputtering in low energy region for various sputtering gases.......................... 19

Figure 2.10 Energy dependence of sputtering yield for copper target ………. 21
Figure 2.11 Incidence angle dependence of sputtering yield for various targets ………………………………………………………… 21
Figure 2.12 Variation of deposition rate with sputtering gas pressure ………. 23
Figure 2.13 Particle flux for ideal sputter source ……………………………. 24
Figure 2.14 Incident particle flux …………………………………………… 24
Figure 2.15 Sputter deposition configurations ………………………………. 25
Figure 2.16 Incident flux variation with polar angle for different deposition geometries …………………………………………………… 26
Figure 2.17 Planetary type substrate holder …………………………………. 27
Figure 2.18 Schematic diagram of capacitive coupled sputtering system …... 28
Figure 2.19 Schematic diagram of magnetic field and electrons' path above magnetron …………………………………………………… 29
Figure 2.20 Photograph of nano-D 100 sputtering system …………………... 30
Figure 2.21 Photograph of the sputtering chamber ………………………….. 30
Figure 3.1 Schematic diagram of multilayer sample ……………………… 32
Figure 3.2 Schematic diagram of single layer sample ……………………… 32
Figure 3.3 Cross sectional TEM images of as sputtered, furnace annealed samples at 600^{o}C, 700^{o}C, 750^{o}C, 800^{o}C for 30 min and SAD of as sputtered and typical SiO_2 samples ………………………….. 34
Figure 3.4 Nanocrystal size dependence on annealing temperature for layer 2, 3 and 4 ……………………………………………………... 35
Figure 3.5 Nanocrystal size distribution of layer 3 ………………………… 36
Figure 3.6 Nanocrystal size distribution of layer 4 ………………………… 37
Figure 3.7 Nanocluster size distribution of layer 5 ………………………… 37
Figure 3.8 Nanocrystal size change with DC power applied to Ge target at various annealing temperatures …………………………………. 38
Figure 3.9 Raman spectra of Ge-L2 ……………………………………….... 40
Figure 3.10 Raman spectra of Ge-L3 ……………………………………….... 41
Figure 3.11 Ge-Ge TO peak shift with annealing …………………………… 41
Figure 3.12 Raman spectra of Ge-L4 ……………………………………….. 42
Figure 3.13 Deconvolved FTIR spectra of as-sputtered SiO_2 ……………… 44
Figure 3.14 Deconvolved FTIR spectra of as-sputtered sample Ge-L4 …….. 44

Figure 3.15 The change in the peak positions with annealing for Ge-L4 45

Figure 3.16 The change in % integrated areas with annealing for Ge-L4 45

Figure 3.17 FTIR spectra of each layer and sputtered SiO_2, Ge-L5, Ge-L4 and Ge-L3 with changing annealing temperature 46

Figure 3.18 Peak position dependence on Ge concentration for as samples ... 47

Figure 4.1 Multilayer sample S1 49

Figure 4.2 Multilayer sample S2 49

Figure 4.3 Two layer sample Si-L series 49

Figure 4.4 TEM image of as-sputtered, annealed at 900^{o}C, 1000^{o}C and 1050^{o}C samples 52

Figure 4.5 SAD of the sample annealed 1050^{o}C 53

Figure 4.6 HRTEM image of the nanocrystal in layer 3 annealed at 1050^{o}C 53

Figure 4.7 Nanocrystal size distribution in layer 3 for annealing at 1000^{o}C and1050^{o}C 53

Figure 4.8 TEM images of upper and lower layers of as-sputtered sample ... 54

Figure 4.9 TEM images of upper and lower layers of annealed sample 54

Figure 4.10 TEM overview of multilayer sample 56

Figure 4.11 Detailed TEM images of each layer 57

Figure 4.12 SAD pattern of annealed S2 58

Figure 4.13 PL spectra of each sample annealed at 1100^{o}C, 3h, N_2 59

Figure 4.14 PL spectra peak position dependence on annealing 60

Figure 4.15 PL spectra integrated area dependence on excess Si concentration 60

Figure 4.16 Hydrogen post annealing effect on PL spectra for sample Si-L2 62

Figure 4.17 PL spectra peak position after H_2 post annealing 62

Figure 4.18 Oxidation of Si nanocrystals in Si-L2 by annealing at 900^{o}C for 10, 20 and 90 min under O_2 63

Figure 4.19 PL peak shift with oxidation of Si nanocrystals for various Si concentration 64

CHAPTER 1

INTRODUCTION

1.1. Motivation

Electronic technology started with invention of the vacuum tubes, accelerated with the transistor and developed with Integrated Circuit (IC) discoveries (Fig 1.1 [1]). Gordon Moore, co-founder of Intel, stated in 1965 that the complexity of IC, in other words density of transistor in a single chip, doubles every two years [2]. Since that time, this observation is the aim of electronic industry. In 1958, first silicon IC had just a few transistors; today ICs have more than a billion transistors in a single chip (Fig. 1.2 [3]). To maintain the increase in density of transistors in a single chip, components' size has to shrink further. Electronics industry must review materials and process steps approaching limits in order to

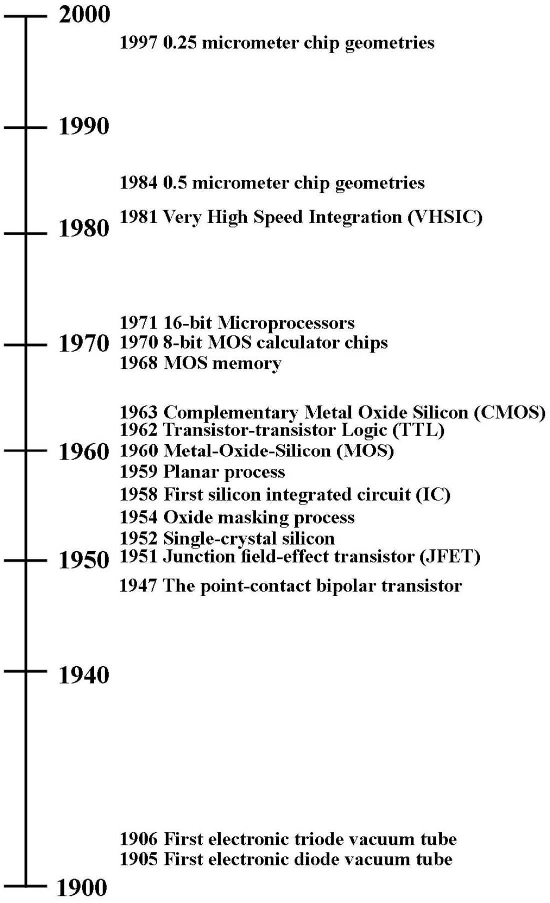

Fig. 1.1 Microelectronics technology evolution timeline

sustain this trend. Nanotechnology is promising to develop new production techniques and novel materials for electronic industry.

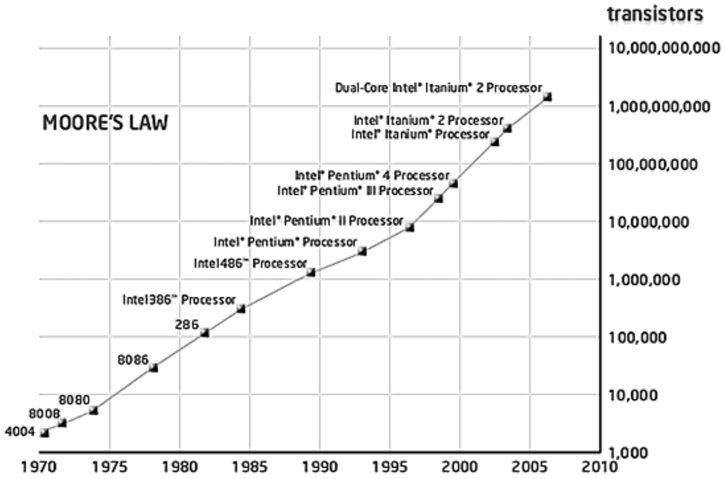

Fig. 1.2 Intel microprocessor evolution timeline

In the last few decades novel materials like nanocrystals, nanorods, nanowires and nanotubes were discovered. Then extensive researches about their properties and applications in electronics were carried out [4-7]. In this thesis fabrication and characterization of germanium (Ge) and silicon (Si) nanocrystals are investigated. In the following sections fabrication techniques, possible applications of Ge and Si nanocrystals in FLASH memories and Light Emitting Diodes (LED), respectively, are explained briefly.

1.1.1. FLASH Memory Application of Germanium Nanocrystals

One of the main issues of Information Technology (IT) is the storage of digital information (0s and 1s). Various forms of storage, based on various natural phenomena, have been invented. Today, optic, magnetic and electronic based memories are the most popular ones. So far no practical universal storage medium has been found since all forms of storage have some drawbacks. Ideal memory basically optimizes the needs of high density, long retention time, fast write/read time, long write/read cycle and low cost.

FLASH type electronic memories are the preferred format in code storage at complex programs running on fast processors and larger media files in portable electronics. Fast write/read operations, long rewrite life, high density and low cost of fabrication are main reasons of this choice. Conventional FLASH cell is basically a Metal Oxide Semiconductor Field Effect Transistor (MOSFET) with a gate completely surrounded by dielectrics as shown in Fig. 1.3 [8].

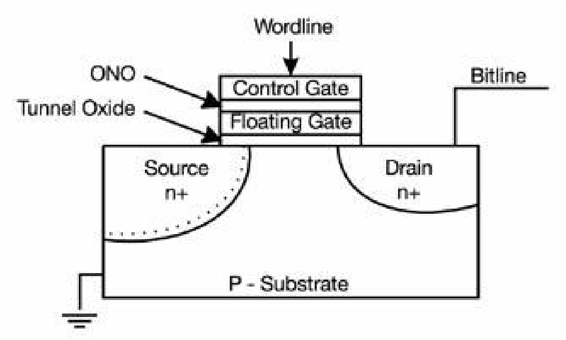

Fig. 1.3 Schematic diagram of conventional floating gate FLASH memory cell

Electrons can be injected into the floating gate through tunnel oxide with Fowler-Nordheim or Direct Tunneling when appropriate voltages are applied to bit line and word line. When the voltages are removed, injected electrons are stored in the quantum well formed with floating gate and surrounding oxides. These electrons modulate the threshold voltage, on/off switching voltage, of transistor. Hence FLASH memory gains the capability of information storage without continuous power supply. Quality and thickness of the tunnel oxide determine the volatility of information stored in the transistor [9].

Conventional continuous floating gate can be replaced by an array of nanocrystals [10] to overcome scaling limitations at FLASH memories as shown in Fig. 1.4. Changing floating gate with Ge nanocrystals provides faster programming and erasing, lower power dissipation and greater reliability [9-11]. Nanocrystal size, their placement in the oxide and oxide thickness are the critical parameters.

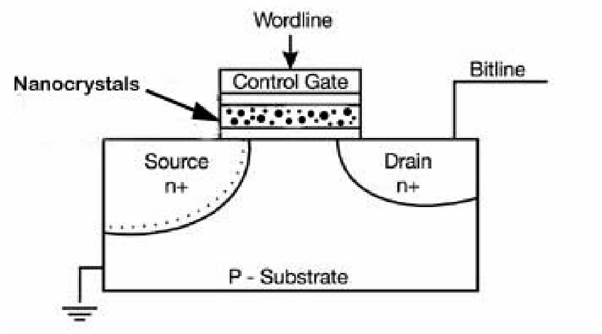

Fig. 1.4 Schematic diagram of nanocrystal based FLASH memory cell

1.1.2. Light Emitting Diode Application of Silicon Nanocrystals

Silicon is the leader of microelectronics with its excellent electronic properties and oxidized form of silicon dioxide (SiO_2). On the other hand indirect band structure of bulk silicon does not allow integration into photonic devices. Today’s photonic devices have been developed on direct band structure II-VI and III-V compound semiconductors. Unfortunately, integration of silicon based microelectronics and II-VI and III-V semiconductor based photonics on the same chip is not feasible.

The observation of efficient photoluminescence from nanocrystalline silicon (nc-Si) at visible region [7] drew great attention for Si based photonics devices and extensive research was carried out in this field [12-14]. Nanocrystalline Si embedded Metal Oxide Semiconductor (MOS) structure can be offered for silicon based LEDs as shown in Fig. 1.5 [15].

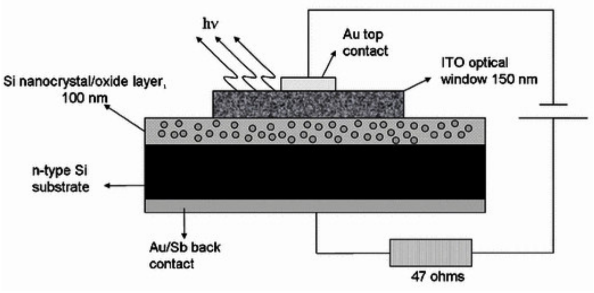

Fig. 1.5 Schematic diagram of Si nanocrystal embedded MOS-LED

1.2. Fabrication of Silicon and Germanium Nanocrystals Embedded in Silicon Dioxide

Precipitation technique is the most popular Si/Ge nanocrystal formation technique. In this technique either silicon dioxide matrix is highly doped with Si/Ge by ion implantation [16, 17] or Si/Ge rich silicon dioxide layer is deposited with chemical vapor deposition [18, 19], laser ablation deposition [20] or magnetron sputtering deposition techniques [21, 22]. When concentration of Si/Ge atoms exceed the solid solubility limit in SiO_2 matrix then these atoms segregate with annealing. This phenomenon can be described by Ostwald ripening of nanocrystals [23]. Two main annealing techniques are the furnace annealing [24] and rapid thermal annealing [25]. Annealing temperature, time and atmosphere are the critical parameters to control the segregation of atoms to nanocrystals.

1.2.1. Ostwald Ripening

W. Ostwald worked on ripening process in biosystems in 1900 and his theory, referred as Oswald Ripening [26], developed [27, 28] and adapted to nanocrystal formation in dielectrics [29]. According to Oswald’s theory small particles are kinetically favored since they nucleate easily; on the other hand big nanocrystals are thermodynamically favored since surface to volume ratio is small. At the beginning of coarsening small clusters form, after the initial growth period larger particles grow at the expense of smaller ones in order to reduce their surface potential energy. Under steady-state conditions rate of atom loss from an individual particle is [26];

$$\frac{dR}{dt} = \frac{2\gamma \overline{V}^2 DC}{kT} \frac{1}{R^2} \left(\frac{R}{\overline{R}} - 1 \right)$$

γ : particle - matrix surface tension
$\overline{V}$: volume per atom in the particle
D : diffusion coefficient in the matrix
C : concentration of precipitate atom at the particle - matrix surface
k : Boltzman constant
T : temperature
R : particle radius
$\overline{R}$: average particle radius

The equation is plotted in Fig. 1.6 [26]. Plot shows that particles of radius $R < \overline{R}$ rapidly dissolve, growth rate of particles of radius $R > 2\overline{R}$ decreases rapidly therefore particles larger than $2\overline{R}$ less probable.

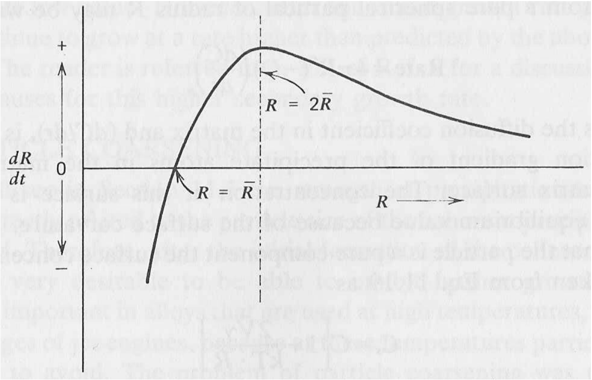

Fig. 1.6 Plot of atom loss from an individual particle

if we solve this differential equation we get;

$$R^3 = R_0^{\ 3} + A\left(\frac{\overline{V}^2 \gamma C D}{kT}\right)t$$

R_0: original mean particle size

R_0 is quite small for coherent precipitates and average particle radius is proportional to one third power of particle-surface tension and equilibrium concentration. Therefore nanocrystal formation enhance with increasing excess particle atoms. Nanocrystals smaller than R shrink and dissolve but larger nanocrystals' size increase.

1.2.2. Ion Implantation Technique

Ion implantation is a surface modification technique used extensively in microelectronics to engineer electrical properties of substrate with impurity atoms. Gas form of the desired element is ionized at the source chamber and electrostatically accelerated at the accelerator line, then implanted to the substrate at the target chamber (see Fig 1.7). Nanocrystals can be formed with precipitation technique by annealing of highly implanted SiO_2 films [16, 17]. Implanted ions per unit area and implantation energy basically determine the concentration of atoms in the SiO_2 matrix. IC technology compatibility, wide range of ions and precise dose control make ion implantation powerful technique for nanocrystal fabrication. On the other hand ion implantation is an ex-situ surface modification technique therefore implantation of complex layered structures is so difficult and low energy implantation is needed for thin oxide implantations. Especially thin control oxide thickness and minimal tunnel oxide degrade requirement of nanocrystal FLASH memory cannot be easily satisfied with ion implantation. Gaussian distribution of implanted ions is another problem in nanocrystal size uniformity but multiple implantations are carried out to overcome this effect [30].

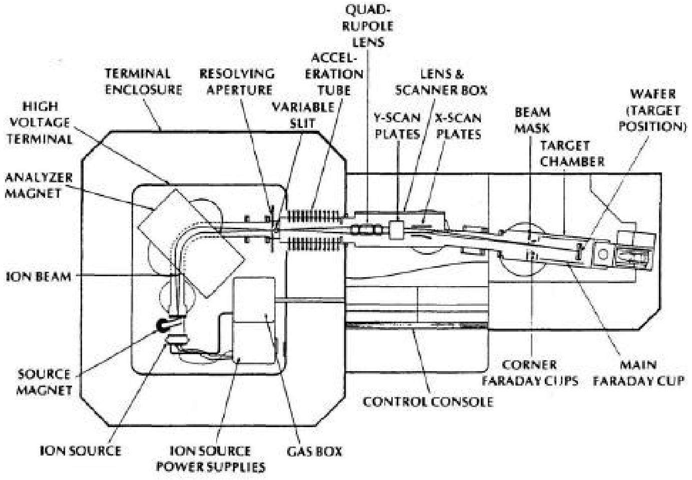

Fig. 1.7 Schematic diagram of an ion implanter system

1.2.3. Chemical Vapor Deposition Technique

Chemical Vapor Deposition (CVD) is a deposition technique used in microelectronics to deposit various forms of thin layers on substrates. Volatile gases introduced to reaction chamber decompose at high temperatures and deposited on the substrate surface to form thin layers (see Fig. 1.8 [31]). Various precursor gases can be used depending on thermal stability of substrate, for example SiO_2 film can be deposited with the following reaction,

$$SiH_4 + O_2 \rightarrow SiO_2 + 2H_2$$

$$SiCl_2H_2 + 2N_2O \rightarrow SiO_2 + 2N_2 + 2HCl$$

$$Si(OC_2H_5)_4 \rightarrow SiO_2 + \text{by products}$$

In the first two reactions silicon to oxygen ratio of silicon dioxide films are determined by the gas flow rates. Flow rates can be varied to obtain silicon rich silicon oxide matrix to form silicon nanocrystals with precipitation technique [18]. Also germanium atoms can be introduced to SiO_2 with the addition of GeH_4, or similar Ge source gas [19]. Decomposed gas type, gas flow rate, background pressure, substrate temperature and deposition time are the critical parameters of this technique. CVD is well suited to mass production.

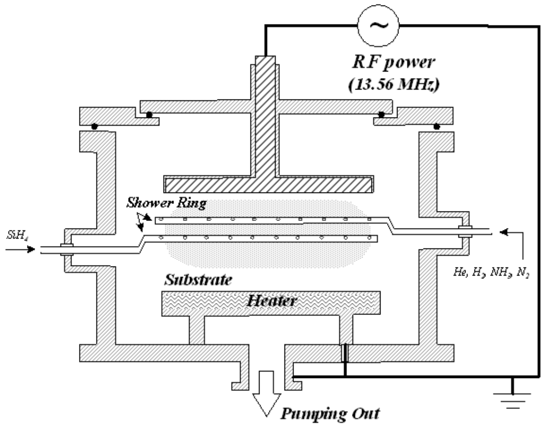

Fig. 1.8 Schematic diagram of a plasma enhanced chemical vapor deposition system

1.2.4. Laser Ablation Deposition Technique

Laser directed on the target absorbs radiation energy and if this energy is high enough the surface layers start to evaporate. A substrate is placed in the view of target material to deposit thin film as shown in Fig. 1.9 [32]. Deposition atmosphere can be inert or a reactive gas can be added depending on the desired film. For example Si rich SiO_2 films can be deposited by ablation of Si targets in oxygen argon mixture background atmosphere. Partial pressure of oxygen determines the concentration of excess Si in SiO_2 matrix [20, 32]. Laser power, spot size, target to substrate distance, deposition atmosphere and ablation time are the critical parameters of this process. The main drawback of laser ablation technique is the lack of control in oxidation of ablated Si atoms.

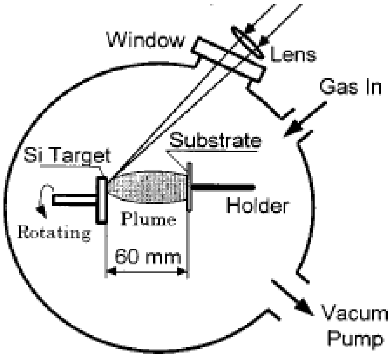

Fig.1.9 Schematic diagram of a laser ablation deposition system

1.2.5. Magnetron Sputtering Deposition Technique

Magnetron sputtering deposition technique is the deposition of target atoms to substrate with the help of plasma ion bombardment. Sputtering gas, commonly argon, ionized and accelerated towards the target and collision of accelerated ions result in momentum and energy transfer hence emission of target's surface atoms. A thin film layer forms on substrate with the condensation of emitted atoms. Si/Ge rich SiO_2 can be deposited by co-sputtering of corresponding targets [21, 22]. Also introducing oxygen into the chamber reactive sputtering of Si target can be carried out to obtain Si rich SiO_2 films [33]. Magnetron sputtering allows the nanocrystal size, density and tunnel oxide thickness control. Details of this technique are explained at Chapter II.

CHAPTER 2

MAGNETRON SPUTTERING DEPOSITION TECHNIQUE

2.1. Sputtering and Its Applications

Sputtering is the bombardment of target material with energetic ions to scatter surface atoms. Energetic ions directed towards the target transfer their energy and momentum to the target's surface atoms via inelastic collisions. Sputtering begins when surface atoms gain energy larger than surface binding energy and momentum out of target's surface. Collision and interaction of target atoms is so complex, cascaded collisions needed to change the momentum angle to out of surface. During these collisions over 95% of ion energy transforms to heat in the target. Sputtering of a crystal target is demonstrated in Fig. 2.1 to give an idea about the cascaded collisions.

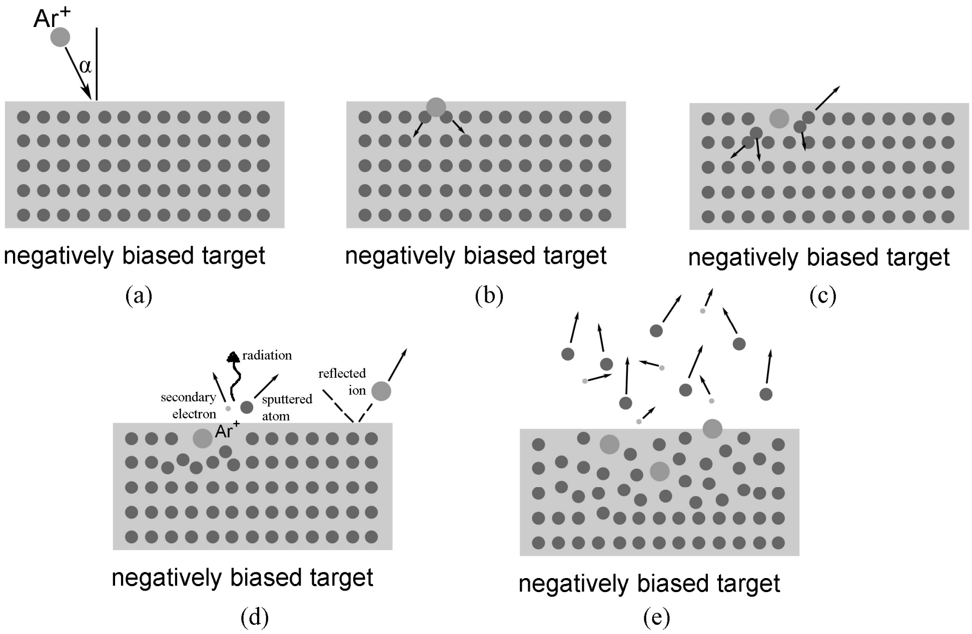

Fig. 2.1 Schematic diagrams of cascaded collusions and sputtering process

Many phenomena take place during sputtering other than neutral particle emission as shown in Fig. 2.1 (d) , these are [34];

- secondary ion emission
- reflection of projectile
- secondary electron emission
- implantation of projectile
- backscattering of sputtered atoms
- radiation
- target heating
- chemical reaction at the target's surface

First two of these phenomena are used to probe the surface of materials in Secondary Ion Mass Spectrometry (SIMS) [35, 36] and Ion Scattering Spectroscopy (ISS) [37], respectively. Sputtering is also used for depth profiling in X-Ray Photoelectron Spectroscopy (XPS), Auger Electron Spectroscopy (AES) [38-40]. Focused Ion Beam (FIB) sputtering is used to micro/nano machine the samples in micro/nano electronics [41, 42]. Moreover sputtering is a well known method to prepare atomically clean the surfaces before deposition [43, 44].

If a sample is placed on view of the sputtered face of target in vacuum then sputtered atoms condense on the sample. This is still an effective way of thin film deposition technique used in integrated circuit technology [45]. A simple schematic of setup is demonstrated at Fig. 2.2 [34].

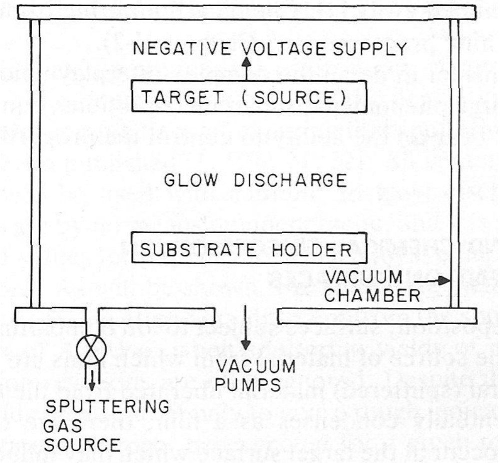

Fig. 2.2 Schematic diagram of a sputtering deposition system

Easy to control film thickness, various sputtering target materials, deposition without compositional changes and mass production compatibility make the sputter deposition powerful thin film deposition technique in IC technology. High temperature melting point targets can easily deposited by sputter deposition. On the other hand slow deposition rates compared to thermal evaporation techniques is the main disadvantage of sputtering.

2.2. Sputtering Parameters

2.2.1. Sputtering Yield

Sputtering yield (Y) is the amount of ejected target atom per incident sputtering ion, in other words efficiency. Sputtering yield determines the erosion rate of target material and gives an idea about film deposition rate. Sputtering yield depends on

- target material
- crystal structure of target
- sputtering gas
- projectile energy
- incidence angle of projectile

2.2.2. Target Material

Sputtering yield may change in the order of 10 for different targets. Experimental yield data and empirical yield curves, suggested by Matsunami et al. [46], of several elemental target materials at1 keV Ar^+ bombardment are shown in Fig 2.3.

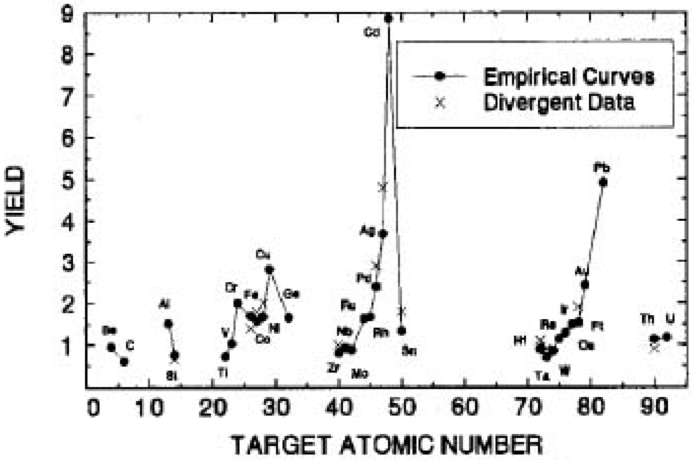

Fig. 2.3. Sputtering yields of several elemental targets at 1 keV Ar^+ bombardment

Some of the experimental data diverges from the empirical curves. Mahan states that "the divergent data points are more often above, rather than below, the empirical curve values. It is our belief that this particular divergence trend is due to the nonlinear cascade, which generates what has been termed an excess yield above that typical of, or even attributable to, the linear cascade sputtering mechanism" [47]. Periodic behaviour of sputtering yield is related to the d-shell fillings of target atoms. Correlation between periodicity of sputtering yield and inverse sublimation energy of targets can be seen by comparing Fig. 2.4 [47] with Fig. 2.3.

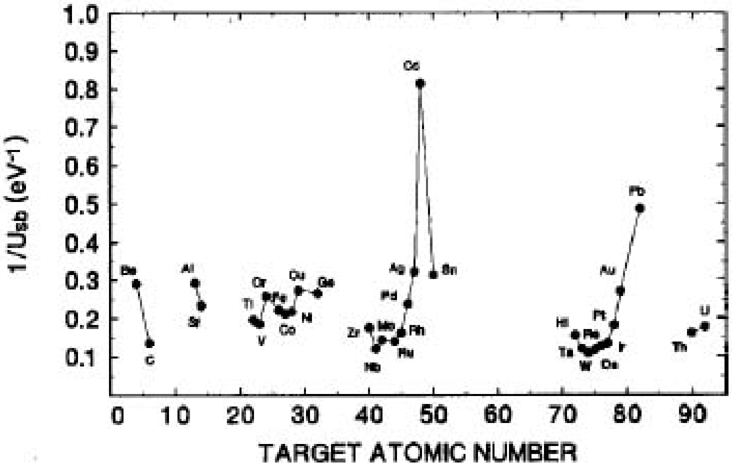

Fig. 2.4. Inverse sublimation energy of several elemental targets

2.2.3. Crystal Structure of Target

Lattice correlated effects like channeling of projectile, blocking of recoils and focusing of collision determines sputtering yield [48]. Sputtering yield dependence of FCC crystals (like Cu, Ag, Au and Al) for energetic Ar^+ obeys $Y_{111} > Y_{poly} > Y_{110}$ relation for few keV is shown in Fig. 2.5 [49].

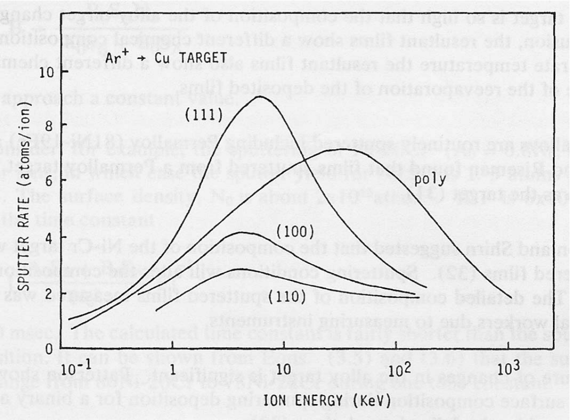

Fig. 2.5 Crystal structure dependence of sputtering yield

Energy transfer of projectile atoms near the surface decreases considerable due to channeling effect. Projectile ions gradually lose their energy due to gentle collisions in the channel and transfer most of their energy to deep layers of crystal instead of the surface. Channeling effect can be observed with changing incidence angle of projectile ions to crystal target as shown in Fig. 2.6 [50].

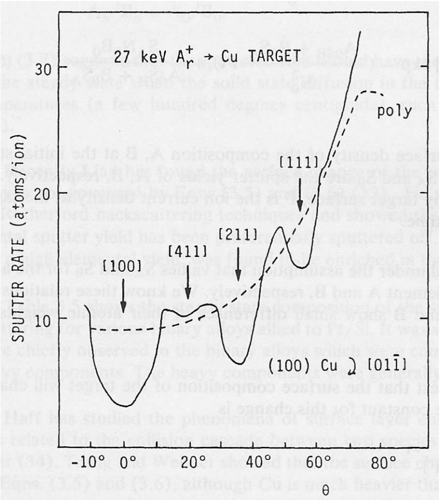

Fig. 2.6 Channeling effect on sputtering yield of Cu (111) target and comparison with polycrystalline Cu target with bombardment of 27 keV Ar^+

2.2.4. Sputtering Gas

Noble gases are used to generate plasma for non-reactive sputtering; Argon is the most common used one. Theoretical [46] and empirical [47] sputtering yields of coulomb IV-B elements are plotted as a function of sputtering gas ions at 1 keV in Fig. 2.7. Sputtering yield increases with increasing projectile mass for heavy targets, on the other hand moderate projectile masses have better sputtering rates for lighter targets.

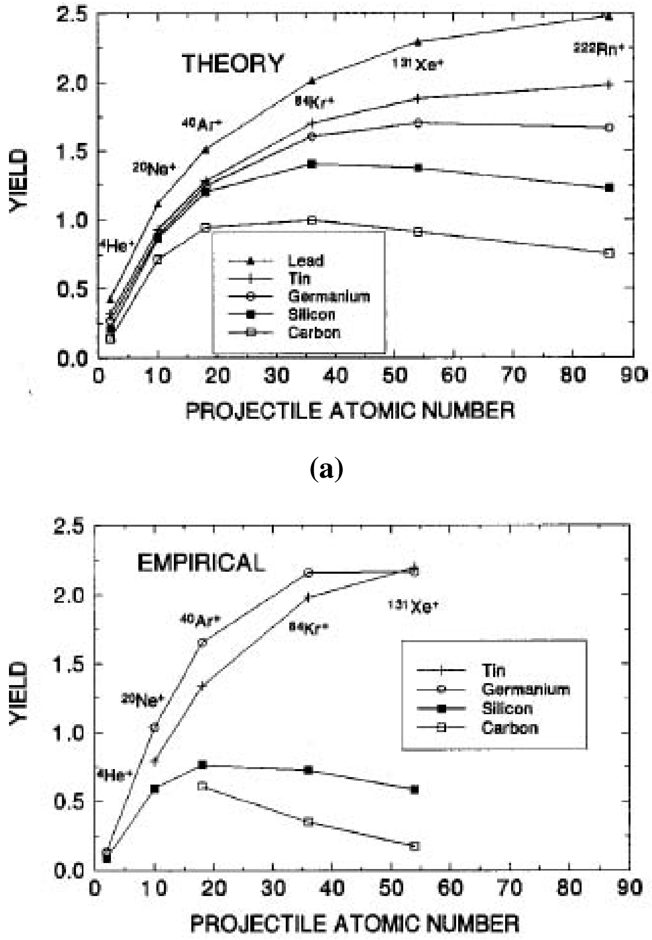

(a)

(b)

Fig. 2.7 Theoretical (a) and empirical (b) sputtering yields of column IV B elements for different noble sputtering gases

Most complete sputtering yield dependence on sputtering gas is reported by Almen and Bruce [51, 52] at 45 keV high energy region for silver, copper and tantalum targets as shown in Fig. 2.8. Sputtering yield shows local maxima at noble gases. It is still an unknown why sputtering gas specie determines the yield more than target properties.

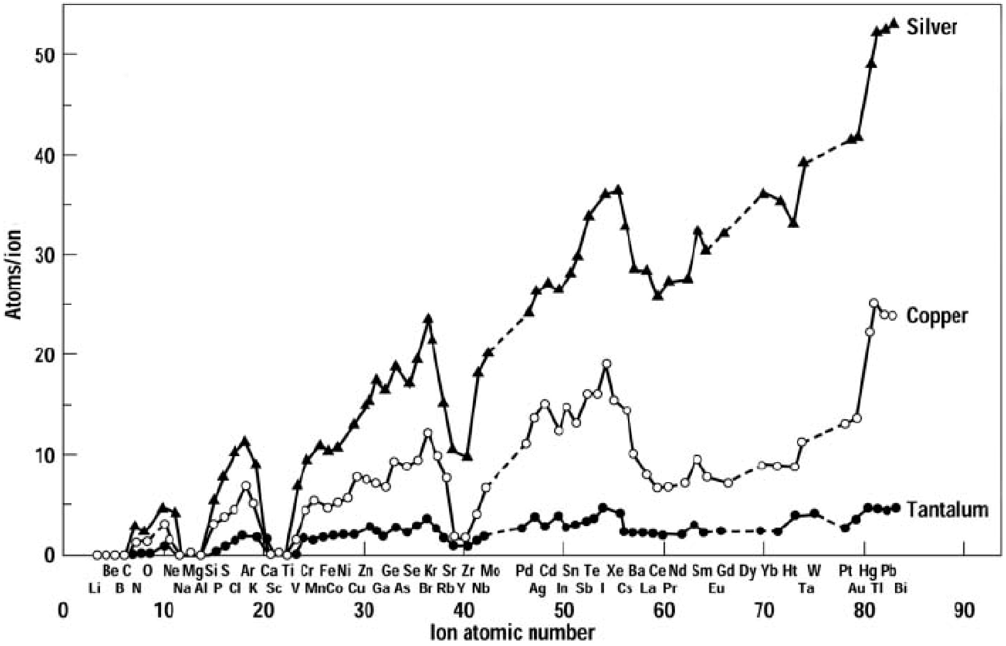

Fig. 2.8 Variation in sputtering yield with sputtering gas

Reactive sputtering is the formation of desired compound on elemental target surface and deposition it to the substrate. In some cases it is used to reinforce the deficient constituent of composite target at the deposited film. Varying ratios of oxide, nitride, sulfide and carbide gases are mixed with noble gas for reactive sputtering.

2.2.5. Projectile Energy

Surface binding energy is the threshold energy to begin sputtering. Spectroscopic techniques are used for sensitive (10^{-4} to 10^{-5} atoms/ion) binding energy measurements. In the low energy region threshold energy and energy dependence of sputtering yield is shown in Fig. 2.9 [53].

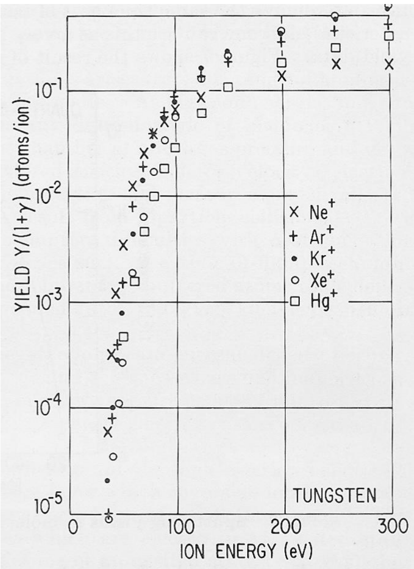

Fig. 2.9. Threshold energy and energy dependence of sputtering in low energy region for various sputtering gases

Threshold energies of various targets are shown in Table 2.1 [53, 54]. Threshold energies of different targets are so close to each other and nearly four times of their heat of sublimation energies.

Table 2.1 Sputtering threshold (eV) and heat of sublimation (eV) data of various elemental targets for different projectiles

Target	Projectile type						
		Ne	Ar	Kr	Xe	Hg	Heat of sublimation
	Al	13	13	15	18	18	-
	Ti	22	20	17	18	25	4.40
	V	21	23	25	28	25	5.28
	Cr	22	22	18	20	23	4.03
	Fe	22	20	25	23	25	4.12
	Co	20	25	23	22	-	4.40
	Ni	23	21	25	20	-	4.41
	Cu	17	17	16	15	20	3.53
	Ge	23	25	22	18	25	4.07
	Zr	23	22	18	25	30	6.14
	Mo	24	24	28	27	32	6.15
	Pd	20	20	20	15	20	4.08
	Ag	12	15	15	17	-	3.35
	Ta	25	26	30	30	30	8.02
	W	35	33	30	30	30	8.80
	Pt	27	25	22	22	25	5.60
	Au	20	20	20	18	-	3.90

A typical sputtering yield dependence of projectile energy curve for copper target and a model developed by Sigmund are shown in Fig. 2.10 [55]. Near threshold energies sputtering yield increases with square of projectile energy. At few hundred eV energy region, sputtering yield is linearly proportional to projectile's energy. At high energy region sputtering yield reaches a maximum and then decreases with increasing projectile energy. Increasing projectile energy results in an increase in the energy transferred to target. Further increase causes increase in implantation of ions which does not contribute to sputtering.

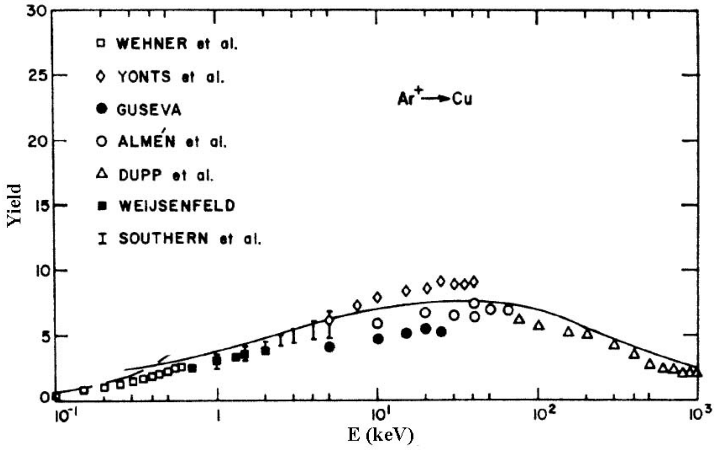

Fig. 2.10 Energy dependence of sputtering yield for copper target

2.2.6. Incidence Angle of Projectile

Sputtering yield changes a little for high yield targets like Ni, W, and Pt with incidence angle of projectile. On the other hand sputtering yield for low yield targets like Mo strongly effected from incidence angle [56] as shown in Fig 2.11. Oblique angle sputtering is much efficient for deposition of Mo and similar targets.

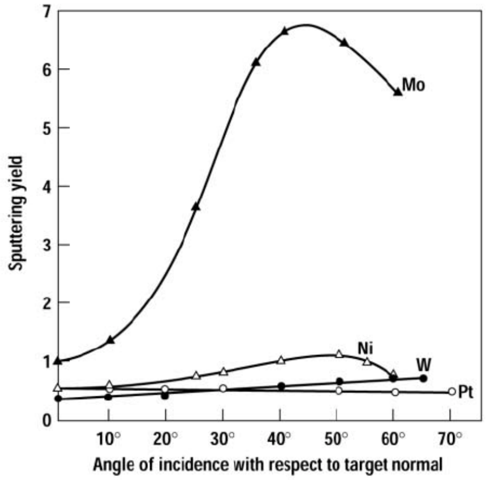

Fig. 2.11 Incidence angle dependence of sputtering yield for various targets

2.2.7. Sputtering Rate

Sputtering rate is the erosion rate of target material. Sputtering rate can be calculated from the ratio of eroded crater depth to the sputter time. Using optical/stylus surface profilers or Scanning Electron Microscopes (SEM) the eroded crater depth can be measured [57]. Unfortunately the depth is not uniform through the crater therefore different depth measurements are averaged. In Table 2.2 ion beam etching rates of different targets using Argon ions at normal incidence are given [58]. Beam current density and accelerating voltage are 1.0 mA/cm^2 and 500 V respectively during ion beam etching.

Table 2.2 Sputtering rate for various targets at 1.0mA/cm^2 Ar$^+$ current density and 500V acceleration voltage

Target	**Rate (Å/min)**
Al (bulk)	300
Si {100}	215
Soda-lime glass	200
SiO_2 (evaporated film)	280
SiO_2 crystal {001}	330
Al_2O_3 { $0\bar{1}02$ }	83

2.3. Film Deposition

2.3.1. Gas Pressure and Power

Sputtering gas pressure effect on deposition rate is shown in Fig. 2.12 [59]. Deposition rate makes a maximum with increasing gas pressure at constant power. Low efficiency in the ion collection of cathode at low pressure and increasing scattering of sputtered atoms with gas ions at high pressure reduce deposition rate.

Sputtering is carried out at gas pressure giving the maximum deposition rate. Desired gas pressure can be controlled either throttling gas inlet or chamber pumping speed. Chamber pumping speed can be controlled by throttling pump inlet or pump speed.

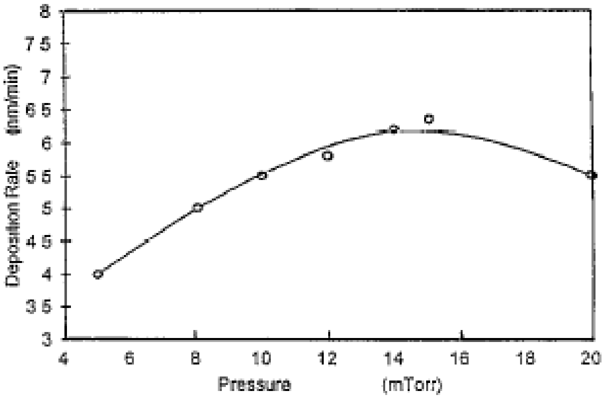

Fig. 2.12 Variation of deposition rate with sputtering gas pressure

During bombardment of target over 95% of ion energy transforms as heat. Therefore target material must be cooled to stay at sputtering regime. Maximum power flux is the limiting factor in both DC & RF magnetron sputtering since exceeding this power results in cracking of target. Thermal conductivity of target and back plate play important roles in cooling rate of target.

2.3.2. Deposition Geometry

Particle flux along the specified direction is the fundamental parameter in physical vapor deposition techniques. Total particle flux for an ideal sputtering point source, i.e. sufficiently small source diameter compared to substrate to target distance, as shown in Fig. 2.13 [48], is

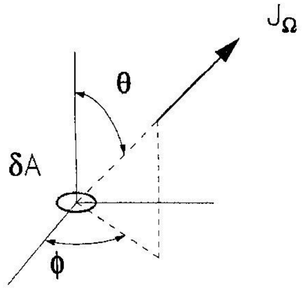

Fig. 2.13 Particle flux for ideal sputter source

$$J_\Omega = \frac{(Yz^+)(\delta A)\cos\theta}{\pi}$$

where

J_Ω: particle flux along solid angle

Yz^+: total particle flux

δA: source area

θ: polar angle

Incident particle flux on deposition surface can be calculated by simple solid geometry, as shown in Fig. 2.14 [48]

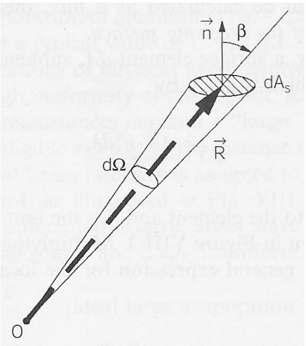

Fig. 2.14 Incident particle flux

$$J_i = \frac{J_\Omega(\vec{R}\cdot\vec{n})}{R^3}$$

$$J_i = \frac{J_\Omega \cos\beta}{R^2}$$

where

J_i: incident particle flux

β: deposition angle

R: target to substrate distance

J_Ω: particle flux along solid angle

Particle flux, substrate to target distance and view angle are important parameters of deposition. Substrate should be as close as possible to target since deposition rate increases with decreasing distance but not enter to plasma region. Typically substrate is located 5-7 cm above the target. Substrate should be placed parallel to target and their axes should coincide to get uniform films.

Three fundamental sputter deposition configurations are illustrated in Fig. 2.15 [48]. These are hemispherical, planar and spherical sputtering deposition configurations.

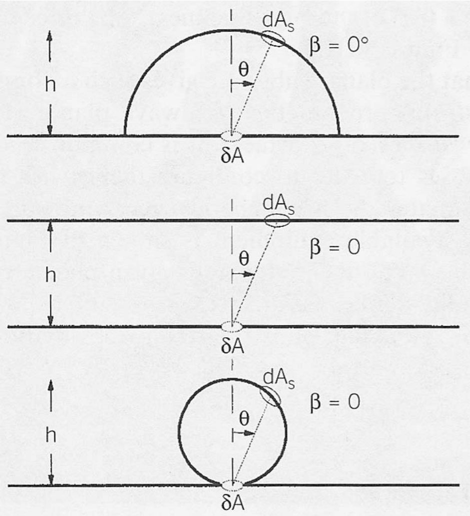

Fig. 2.15 Sputter deposition configurations

1. Incident particle flux for hemispherical configuration is

$$J_i = \frac{z\delta A \cos\theta}{\pi h^2}$$

2. Incident particle flux for planar configuration is

$$J_i = \frac{z\delta A (\cos\theta)^4}{\pi h^2}$$

3. Incident particle flux for spherical configuration is

$$J_i = \frac{z\delta A}{\pi h^2}$$

Incident flux variation with polar angle for each configuration is illustrated in Fig 2.16 [48]. Tangential spherical configuration has the advantage of polar angle independence but just small substrates can be deposited in this configuration. On the other hand planar configuration is the most polar angle dependent geometry but commonly used due to mass production compatibility.

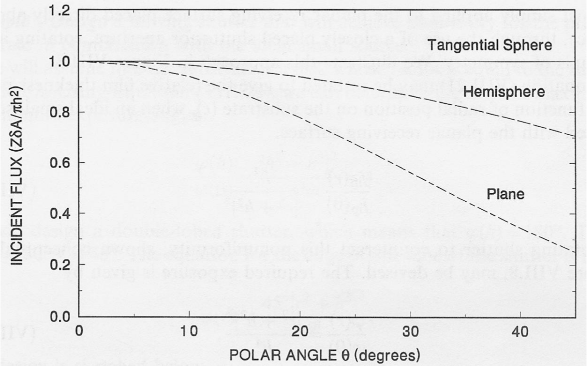

Fig. 2.16 Incident flux variation with polar angle for different deposition geometries

Static substrate deposition configurations cause nonuniform films therefore substrates make planetary or other rotary motions relative to target when high uniformity is necessary, a photograph of such a holder shown in Fig. 2.17 [34].

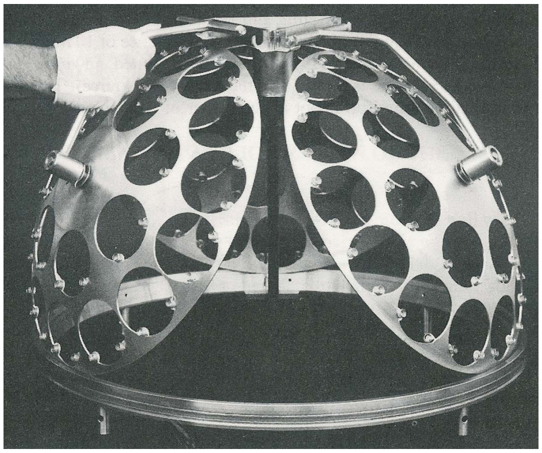

Fig 2.17 Planetary type substrate holder

2.3.3. Condensation Efficiency

Condensation coefficient (α_c) is the ratio of condensation flux to incident flux

$$J_c = \alpha_c J_i$$

Condensation coefficient is near to unity for strongly bonded elements but far less than unity for ionic, complex or anisotropic solids. Condensation coefficient depends on the substrate surface, substrate temperature and previously condensed material [48].

2.3.4. Substrate Heating

Magnetron sputtering is a low temperature deposition technique compared with e-beam evaporation or chemical vapor deposition techniques. Secondary electron bombardment, sputtered atom kinetic energy, heat of condensation and radiation are the main sources of substrate heating. Substrate is negatively biased to overcome electron bombardment and cooled to reduce substrate heating effects. Substrate can be heated to increase surface mobility and step coverage of deposited material. Substrate heating also affects optical and electrical properties of deposited films.

2.4. Experimental Method and Setup

2.4.1. DC & RF Sputtering

Capacitive coupled sputtering is the most commonly used sputtering arrangement. In this system target is cathode and substrate is anode facing to the cathode (see Fig. 2.18 [34]). Variable DC / RF (most commonly 13.56 MHz) power supply is used to accelerate the ions toward the target. In the RF case blocking capacitor and matching network is necessary to develop DC self bias and optimize power transfer from RF supply to plasma. RF sputtering has advantageous of having high deposition rates, sputtering of insulating targets, low power and low pressure operation conditions. In some configurations substrate is also negatively biased to clean substrate surface before deposition. Substrate may be heated or cooled depending on configuration but cathode must be cooled during sputtering. Substrate moves relative to target in some configurations in order to get better film uniformity or to prepare complex film. Turbo molecular, diffusion or sublimation pumps are used to reach low base pressure before sputtering. Inlet gas or gas mixtures introduced to the chamber by gas flow controllers. Process gas pressure ranges from a few militorr to few hundred militorrs. Plasma is sustained by secondary electron ejection from cathode and impact ionization of neutral gas atoms.

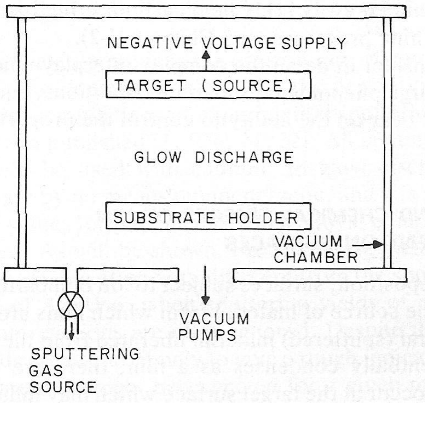

Fig. 2.18 Schematic diagram of capacitive coupled sputtering system

2.4.2. Magnetron Sputtering

Magnetic field is added to sputtering systems in 1970 to increase deposition rate. Magnetic field is used to sustain and increases the ion density in the plasma by trapping electrons near target surface. Hence low pressure sputtering (up to 10^{-5}torr) with high deposition rate can be performed. Permanent or electromagnets are used at different geometries to obtain uniform magnetic fields parallel to the target's surface and perpendicular to electric field so electrons follow circular and spiral path as shown in Fig. 2.19 [34].

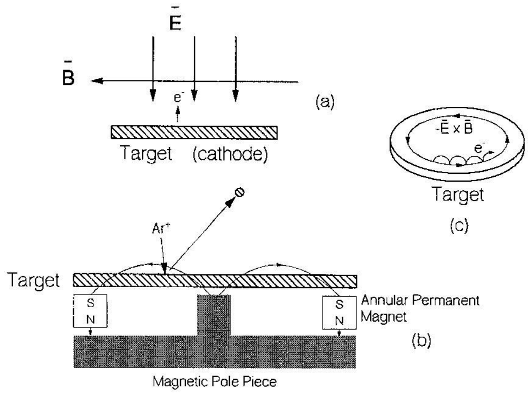

Fig 2.19 Schematic diagram of magnetic field and electrons' path above magnetron

2.4.3. nano-D 100

nano-D 100 is a multi target capacitive coupled DC & RF magnetron sputtering system manufactured by Vaksis ltd. (see Fig. 20 and 21). Complex structures and compounds can be prepared using three 3 inch circular magnetrons installed. One of the magnetrons is connected to 600W 13.56MHz RF supply other two are 500W and 1kW DC supplies; hence various conductors and insulator can be co-sputtered. Up to 2 inch substrates can be mounted on circular rotating substrate holder. Target to substrate distance and angle is adjustable. Base pressure up to 10^{-7} Torr can be achieved with installed Turbo Molecular Pump (TMP). Argon is used for sputtering gas and reactive sputtering can be performed with 3 channel controlled gas inlet. High purity oxygen and nitrogen gases are installed to the system. Substrate can be heated before or during deposition via infrared heater from the back side up to 1000°C. Deposited film thickness is monitored with a crystal oscillator.

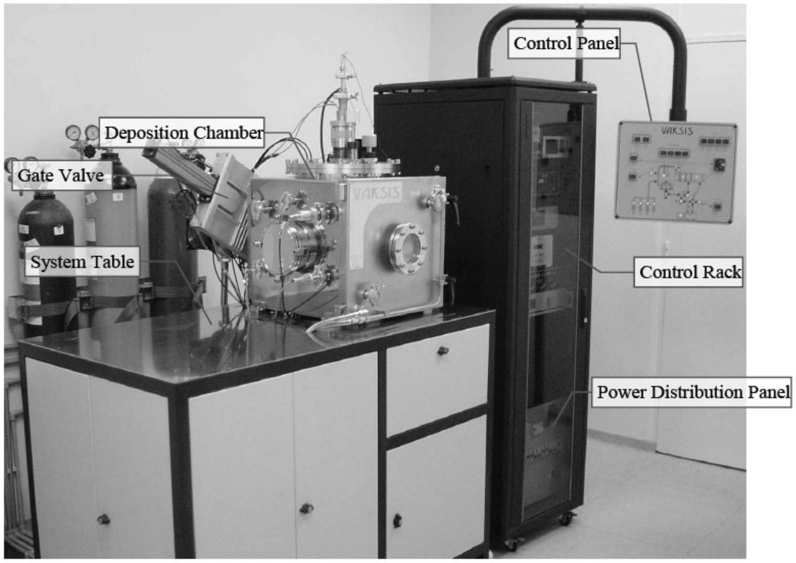

Fig. 2.20 Photograph of nano-D 100 sputtering system

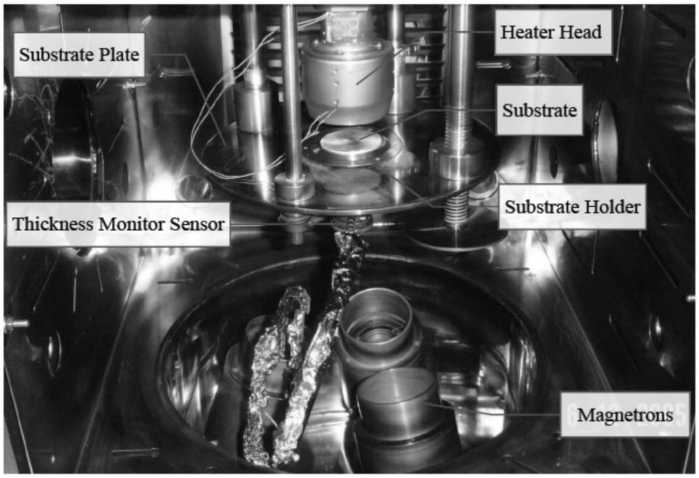

Fig. 2.21 Photograph of the sputtering chamber

CHAPTER 3

SYNTHESIS AND CHARACTERIZATION OF GERMANIUM NANOCRYSTALS

3.1. Sample Preparation

n-type Si (100) substrate with 40 nm thick thermally oxidized SiO_2 top layer was subjected to standard Si surface cleaning procedure. Sample was heated at 500°C for 20 minutes under vacuum in the sputtering chamber in order to remove residual contamination and water molecules at its surface. The base pressure of the chamber was $7x10^{-7}$ Torr before the deposition. The multilayer Ge+SiO_2 thin films were deposited at room temperature by co-sputtering method from 3 inch diameter Ge (99.999% pure) and 3 inch diameter SiO_2 (99.995% pure) targets in Argon ambient using Vaksis nano-D 100 sputtering system. Ge concentration of the layers was controlled with the magnitude of applied DC power to the Ge and RF power to SiO_2 targets. The thicknesses of the films were controlled with sputtering time. Details of process parameters are listed in Table 3.1. Sputtering pressure was fixed at 3 mTorr during the depositions.

Table 3.1 Sputtering conditions of multilayer and single layer samples

Layer #	Sample name	Ge target power (W)	SiO_2 target power (W)	Sputter time (min)	Argon pressure (mTorr)
5	Ge-L5	4	175	24	3.00
4	Ge-L4	11	175	20	3.00
3	Ge-L3	22	175	14	3.00
2	Ge-L2	55	175	8	3.00
1	-	66	0	10	3.00

Multilayer films (see Fig. 3.1) with gradually decreasing Ge concentration were deposited on the substrate for Transmission Electron Microscopy (TEM) measurements. In addition, single layer films with the same Ge concentration as in the multilayer structure were deposited as shown in Fig. 3.2 for Fourier Transform Infrared (FTIR) and Raman spectroscopy measurements. The single layer samples were named as Ge-L2, Ge-L3, Ge-L4 and Ge-L5 referring to each corresponding layer of multilayer sample (see Table 3.1).

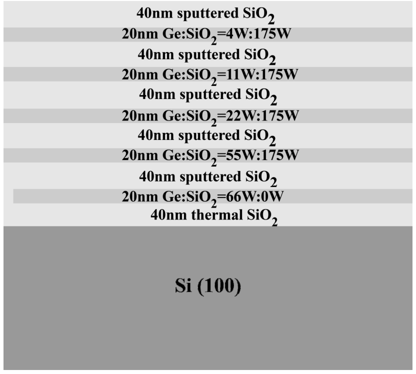

Fig. 3.1 Schematic diagram of multilayer sample

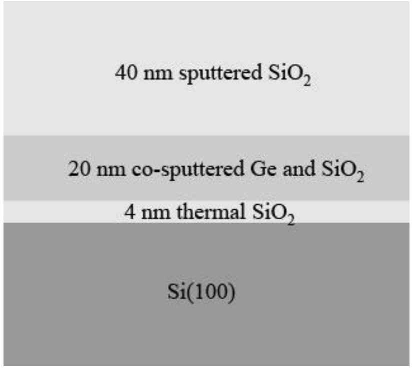

Fig. 3.2 Schematic diagram of single layer sample

Multilayer and single layer samples were cut into pieces and annealed in fused quartz furnace at 600^{o}C, 700^{o}C, 750^{o}C and 800^{o}C temperatures under vacuum (3.4x10^{-5} Torr) for 30 minutes.

3.2. Transmission Electron Microscopy

Various methods have been used to study nanocrystals, but TEM is the most powerful technique to measure nanocrystals' shape, size distribution, density and location in the matrix. On the other hand, extremely careful sample preparation steps and high operation costs do not allow analysis of large number of samples.

3.2.1. Instrumentation

TEM measurements were carried out with 200 keV analytical JEOL2000FX. Cross sectional TEM specimens were prepared by standard procedure, i.e. each sample is cut into pieces with diamond saw then two of the pieces are glued together with deposited layers facing each other, it is then mechanically thinned and finally thinned down to electron transparency by ion milling.

3.2.2. Measurements and Discussion

No single particle can be distinguished in any layer of the as-sputtered sample's TEM image as shown in Fig. 3.3a. Selected Area Diffraction (SAD) patterns indicate the presence of amorphous Ge in the SiO_2 matrix (see Fig. 3.3f), since sample is deposited at room temperature.

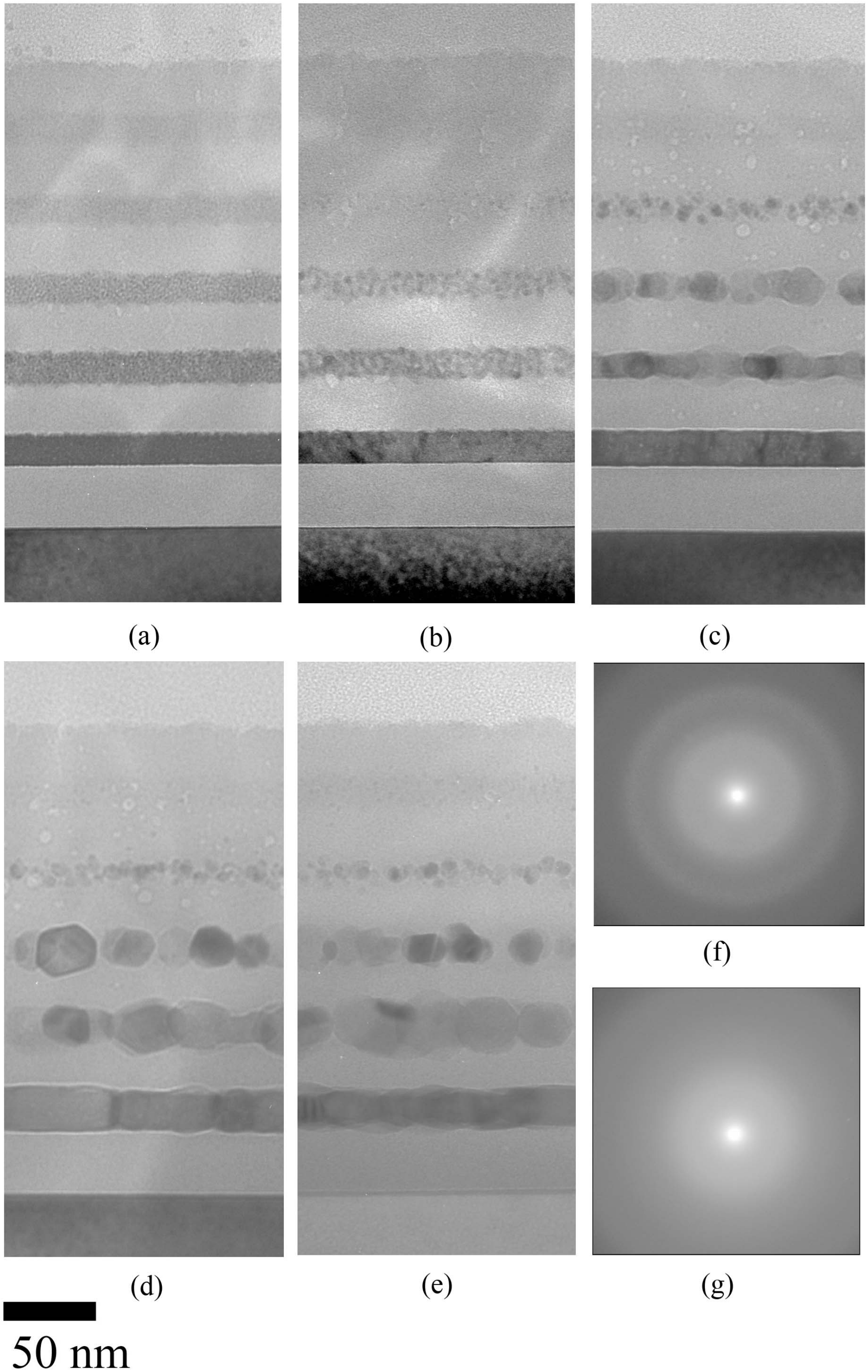

Fig. 3.3 Cross sectional TEM images of (a) as-sputtered, furnace annealed at (b) 600^{o}C, (c) 700^{o}C, (d) 750^{o}C, (d) 800^{o}C for 30min and SAD of (f) as sputtered and (g) typical thermal SiO_2 sample

As expected, layer 1 (%100 Ge) turned into a polycrystalline film after annealing. Nanocrystal formation started at as low as 600°C in layers 2, 3 and 4. Nanocrystal sizes are plotted with respect to annealing temperature for these layers in Fig. 3.4.

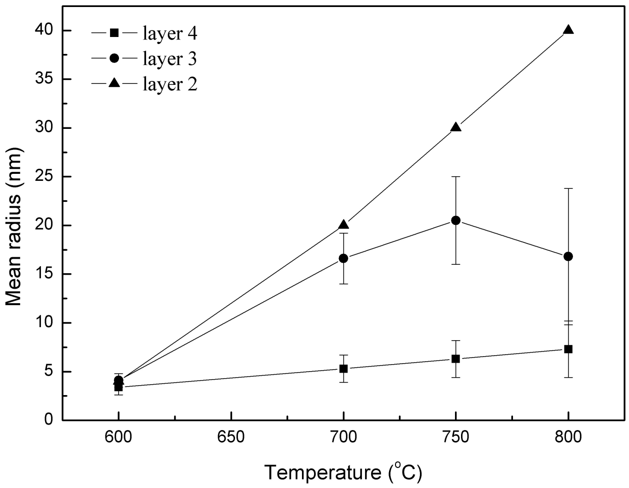

Fig. 3.4 Nanocrystal size dependence on annealing temperature for layer 2, 3 and 4

Due to high Ge concentration in layer 2, nanocrystal size increases dramatically with increasing annealing temperature (see Fig. 3.4) and even exceeds the deposited layer thickness (see Fig. 3.3). It is interesting that big nanocrystals with 20-40 nm size deform probably due to nonuniform compressive silicon dioxide stress and take elongated and faceted forms [60]. Well separated nanocrystals can be observed in layer 3 at the TEM images. As seen in Fig. 3.4, nanocrystal size increases drastically with increasing annealing temperature up to 750°C and decreases at 800°C which was also reported by Choi et al. [61]. Meanwhile variation in the size of nanocrystals increases with annealing. Frequency distribution of nanocrystal size is plotted in Fig. 3.5. Again large nanocrystals with sizes comparable with layer thickness deformed due to high oxide stress.

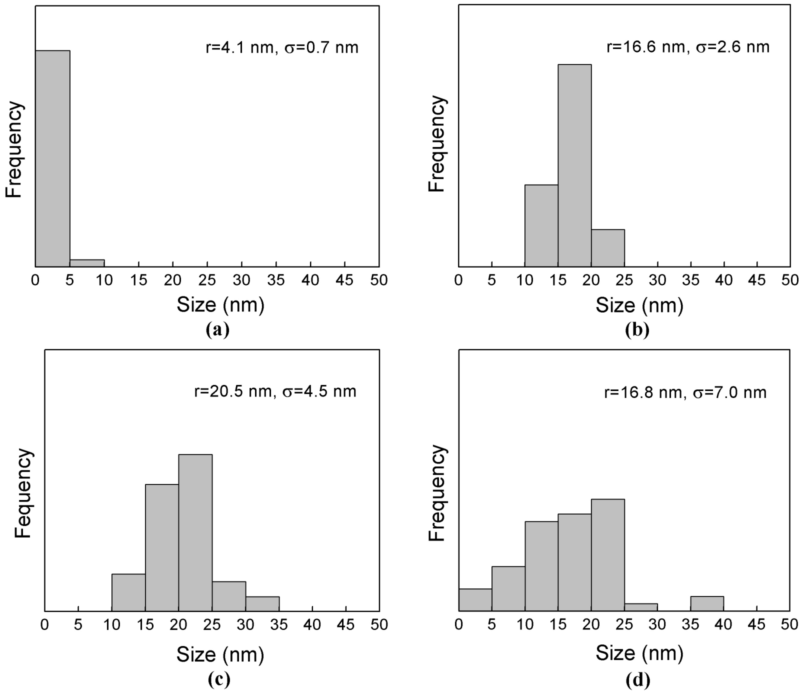

(a) (b) (c) (d)

Fig.3.5 Nanocrystal size distribution of layer 3

Well separated and uniformly distributed spherical nanocrystals are observed in layer 4 (see Fig. 3.3). It is seen from Fig. 3.4 that and nanocrystals size increases with increasing annealing temperature smoothly and the size variation is small. Ge nanocrystal formation is much controllable in this layer. Frequency distribution of nanocrystal size is plotted in Fig. 3.6. The mean nanocrystal size is between 3-8 nm which is reported to be the optimum nanocrystals size for FLASH memory applications [62-64].

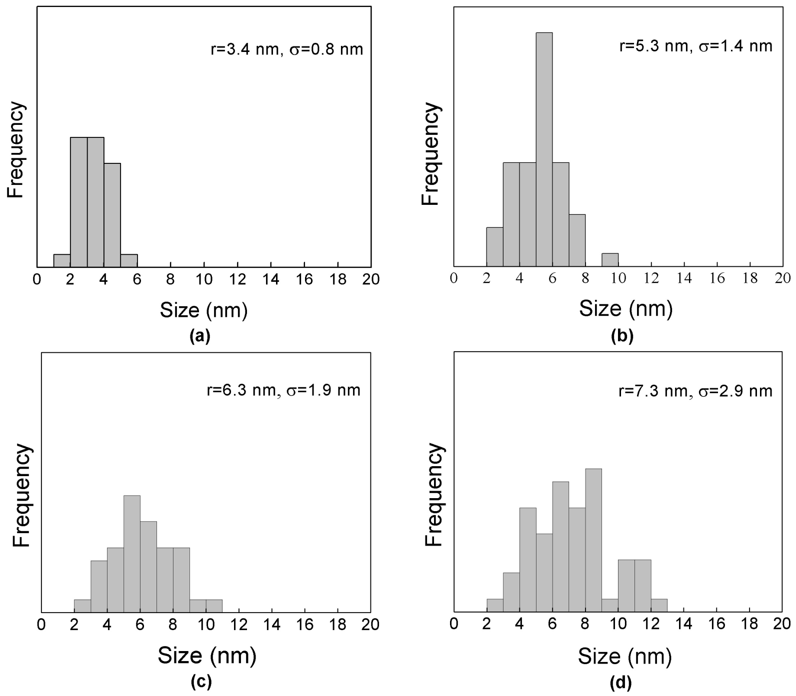

Fig. 3.6 Nanocrystal size distribution of layer 4

Ge concentration in layer 5 is not sufficient for precipitation at temperatures lower than 800°C and at 800°C excess Ge atoms form small nanoclusters but not in crystal form. Frequency distribution of nanocluster size is plotted in Fig. 3.7.

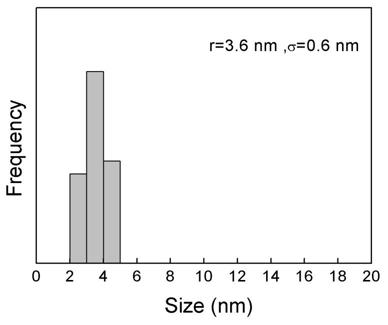

Fig. 3.7 Nanocluster size distribution of layer 5

The variation of the nanocrystal size with the DC power applied to Ge target at various annealing temperatures is plotted in Fig. 3.8.

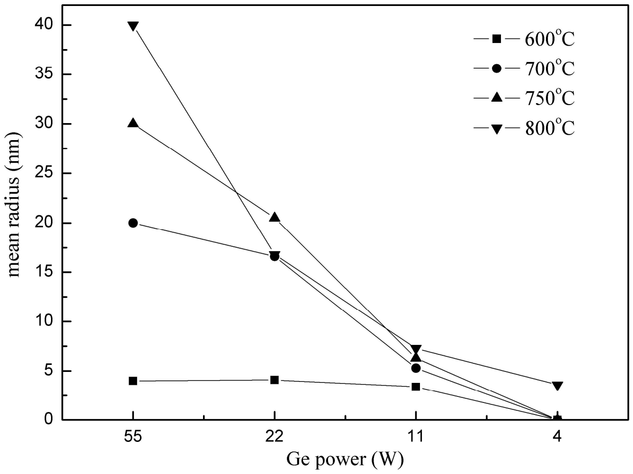

Fig. 3.8 Nanocrystal size change with DC power applied to Ge target at various annealing temperatures

Another important point is the position of Ge nanocrystals in the SiO_2. It is well known that Ge atoms diffuse rapidly in the oxide films at temperatures near and above melting point of Ge (937^{o}C) and segregates to Ge+SiO_2/Si interfaces [65] or diffuse inside the SiO_2 layer [66]. Also Ge segregation to Ge+SiO_2/SiO_2 was observed even at 800^{o}C [67]. In layer 4 segregation to Ge+SiO_2/Si is not observed at any temperature. We observed that both in layer 2 and 3 Ge nanocrystals were sandwiched between SiO_2 layers. These layers play an important role in the nanocrystals' size [63]. Ge in SiO_2 behaves as a modifier not a network former; therefore mobility of Ge in co-sputtered layer is much higher than that of just oxide layers. Hence SiO_2 layers behave as diffusion barrier during nanocrystal growth. Chew et al. state that "the maximum size of the nanocrystals correlates well to the Ge+SiO_2 layer thickness at low concentration samples. However, when the Ge concentration was increased relative to the oxide concentration, the size control over the synthesized nanocrystals was not effective" [67]. Moderate Ge concentration in layer 3 is the cause of nanocrystal size correlation with layer thickness but in layer 2 due to high Ge concentration size control over nanocrystals can not be achieved.

It is interesting to note that voids are observed in the oxide both in as sputtered sample and in the annealed samples. Voids take spherical forms probably to minimize the compressive oxide stress.

3.3. Raman Spectroscopy

Raman spectroscopy is a fast, powerful and non-destructive technique to analyze nanocrystals. Ge-Ge bond vibrations give the information on phase change of Ge from amorphous to crystalline state, stress evolution on nanocrystals [68] and size variation of Ge nanocrystal [69].

3.3.1. Instrumentation

Backscattering Raman measurements were carried out with Jobin Yvon Horiba confocal micro-Raman at room temperature. He-Ne laser with 632.83 nm was used as an excitation source, double monochromator and Peltier cooled CCD detector with a resolution less than 1 cm^{-1} was used to detect Raman shifts.

3.3.2. Measurements and Discussion

Ge nanocrystal formation in the single layer samples was investigated by Raman spectroscopy. As expected, as-sputtered samples show no indication of nanocrystal formation at any concentration. A small asymmetric peak emerges at 298 cm^{-1} indicating the formation of Ge nanocrystals upon annealing at 600^oC of Ge-L2 as seen in Fig. 3.9. The peak intensity increases dramatically with an asymmetric broadening over low frequency side of the spectrum. Broad Si Longitudinal Optical (LO) peak contribution to Ge signal at 301 cm^{-1} [70] is negligible in these measurements. Decreasing Full Width at Half Maxima (FWHM) with increasing temperature indicates change from small to large diameter nanocrystals [69]. It was shown that Ge-Ge Transverse Optical (TO) peak shifts to higher frequencies with increasing nanocrystal size due to phonon confinement effect [69, 71, 72]. On the other hand, stress induced on Ge nanocrystals in SiO_2 matrix result in shift to lower frequencies [73, 74]. Low frequency shift with increasing nanocrystal size competes with high frequency shift with stress. In TEM images both effects can be observed and in Raman measurements they cancel each other and no shift can be observed at Ge-Ge TO peak.

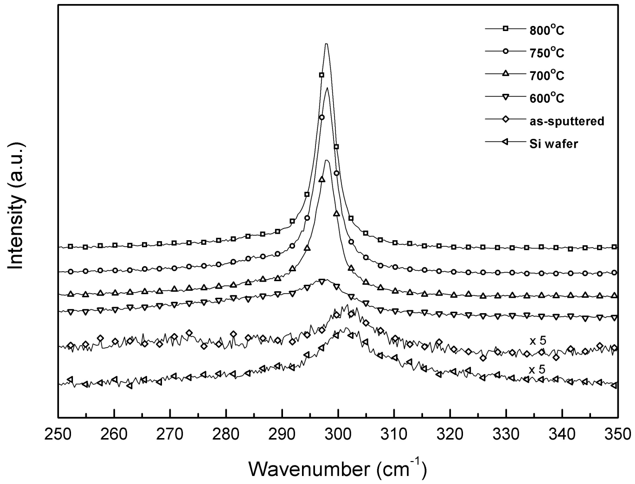

Fig. 3.9 Raman spectra of Ge-L2

In the sample Ge-L3, a small peak appears at 300 cm^{-1} with annealing at 600°C indicating the formation of Ge nanocrystals. Upon increasing the temperature to 700°C and 750°C, the intensity increases gradually then decreases at 800°C. As seen from Fig. 3.10 Si LO peak fixed is at 301 cm^{-1} while Ge-Ge TO signal shifts to lower frequencies with increasing annealing temperature up to 750°C then shifts to high frequency at 800°C. This behaviour was also observed by Choi et. al. [61]. Variation of the Ge-Ge TO peak position with annealing temperature (see Fig. 3.11) is in correlation with the variation of nanocrystal size see Fig. 3.4). Stress effect dominates at Ge-Ge TO peak position in competition with the phonon confinement effect [68].

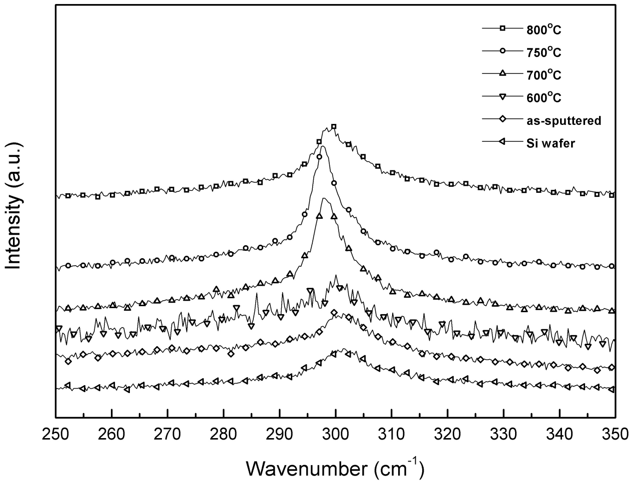

Fig. 3.10 Raman spectra of Ge-L3

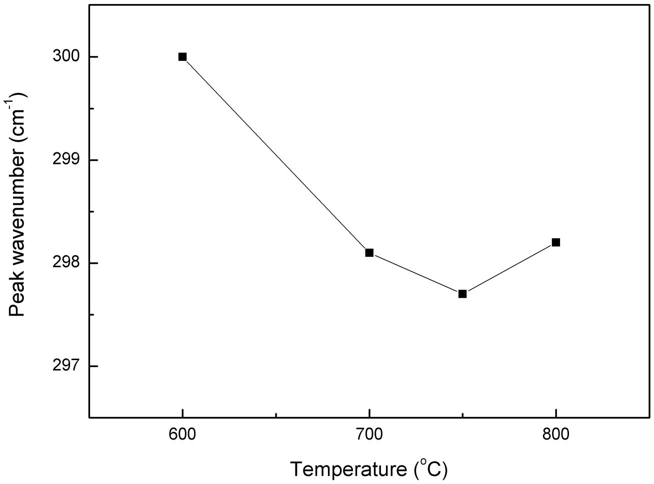

Fig. 3.11 Ge-Ge TO peak shift with annealing

When the Ge content is reduced (sample Ge-L4) no indication of nanocrystal formation is observed in the Raman spectra. The peak seen at 301 cm^{-1} in this sample belongs to the Si substrate (see Fig. 3.12). However TEM pictures show formation of nanoclusters and SAD verifies that there are crystalline nanostructures in this layer. The lack of Raman signal might be due to the low density of Ge nanocrystals in SiO_2 matrix. The weak Raman signal might have been lost in the Si LO signal.

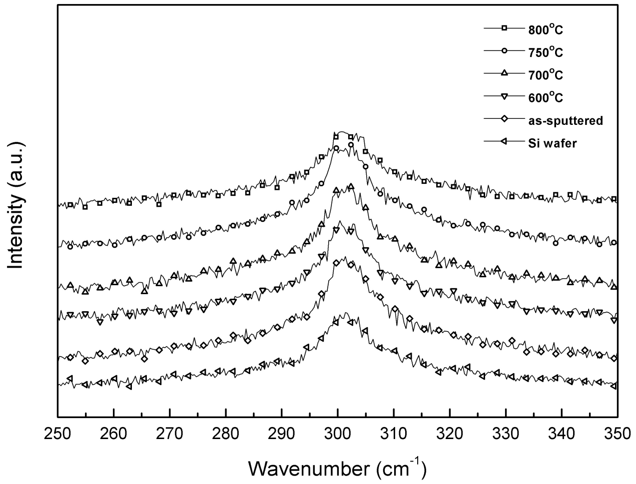

Fig. 3.12 Raman spectra of Ge-L4

3.4. Fourier Transform Infrared Spectroscopy

FTIR spectroscopy is a fast, powerful and non-destructive technique to analyze SiO_2 matrix evolution during Ge nanocrystal formation. Si-O-Si bond vibrations give the information on recovery of SiO_2 matrix as result of decomposition of GeO_x and formation of Ge nanocrystals. In this way Ge nanocrystal formation can be investigated with FTIR spectroscopy indirectly.

3.4.1. Instrumentation

FTIR measurements were carried out with Bruker Equinox 55 FTIR in absorbance mode at room temperature. The FTIR spectrum of the samples was measured with respect to bulk Si from 400 to 4000 cm^{-1} with a resolution of 4 cm^{-1} at 40^{o} angle of incidence with unpolarized light. 50 Measurements were averaged to smooth data.

3.4.2. Measurements and Discussion

In literature rocking, bending and asymmetric stretching mode of Si-O-Si was reported near 459 cm^{-1} (TO$_1$), 815 cm^{-1} (TO$_2$), 1081 cm^{-1} (TO$_3$) [75]. Since the influences of Ge nanostructures on rocking and bending modes are too weak to discuss, only asymmetric stretching mode at 1081 cm^{-1} will be concerned. If the film thickness is comparable with the wavelength of excitation source, longitudinal optical (LO) resonances can be observed with oblique angle incidence configuration [76]. These additional vibrational modes are 1253 (LO$_3$), 1161 (LO$_4$) and 1205 (TO$_4$) cm^{-1}, as shown in Fig. 3.13. Kirk [77] related these peaks with disorder-induced mode coupling in amorphous SiO$_2$. 1253 cm^{-1} (LO$_3$) and 1161 cm^{-1} (LO$_4$) are the longitudinal optical resonance parts of LO-TO splitting of asymmetric stretching modes at 1081 cm^{-1} (TO$_3$) and 1205 cm^{-1} (TO$_4$) respectively [75, 77]. Adjacent oxygen atoms move in phase in 1081 cm^{-1} mode, while they move out of phase in weak 1205 cm^{-1} mode [75].

A deconvolved FTIR spectrum of as-sputtered SiO2 was used as a reference to understand variation of the matrix with Ge concentration and annealing temperature, (see Fig. 3.13). When the same deconvolution procedure is applied to the as-sputtered sample Ge-L4, SiO$_2$ spectra shifts to lower wave numbers and a new peak rises at 971 cm^{-1} as seen in Fig. 3.14. This peak is related to Si-O stretching vibration in SiO$_x$ ($x < 2$) [78]. The presence of the excess Ge in forms of GeO$_x$ and GeO$_2$ [79] result in inhomogeneous SiO$_x$ matrix formation. The non-stoichiometric matrix starts to recover as excess Ge atoms precipitate to form nanocrystal during the annealing [80]. TO$_3$ peak shifts to 1083 cm^{-1} with increasing integrated area and LO$_3$ shifts to 1242 cm^{-1} with a constant integrated area with increasing annealing temperature. Meanwhile SiO$_x$ peak shifts to lower wavenumbers with decreasing integrated area as shown in Fig. 3.15 and Fig. 3.16. In the Ge and SiO$_2$ co-sputtered films Si–O–Si, Ge-O and Si–O–Ge bonds exist, the Ge–O bond (6.8 eV) is weaker than Si–O (8.3 eV) therefore can be broken easily [81, 82]. With increasing annealing temperature GeO$_x$ ($x \leq 2$) decomposes [79] and oxygen atoms bind themselves to SiO$_x$ to form SiO$_2$. Ge nanocrystal formation and the recovery of the SiO$_2$ are in agreement with the TEM results.

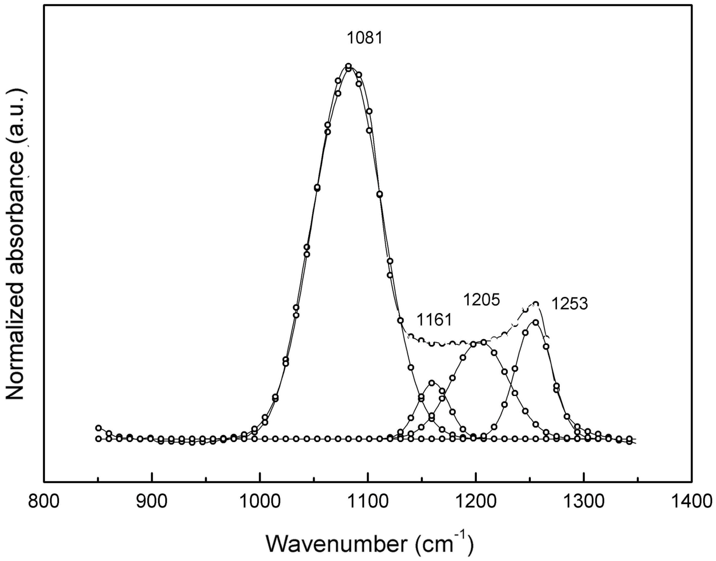

Fig. 3.13. Deconvolved FTIR spectra of as-sputtered SiO_2

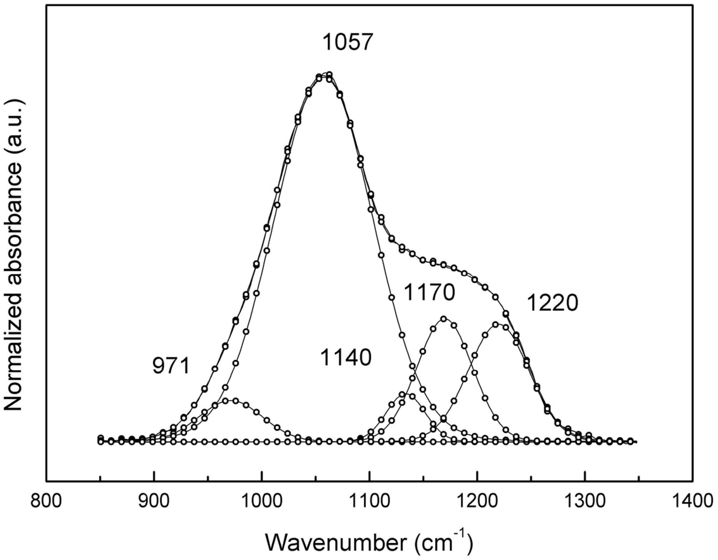

Fig. 3.14 Deconvolved FTIR spectra of as-sputtered sample Ge-L4

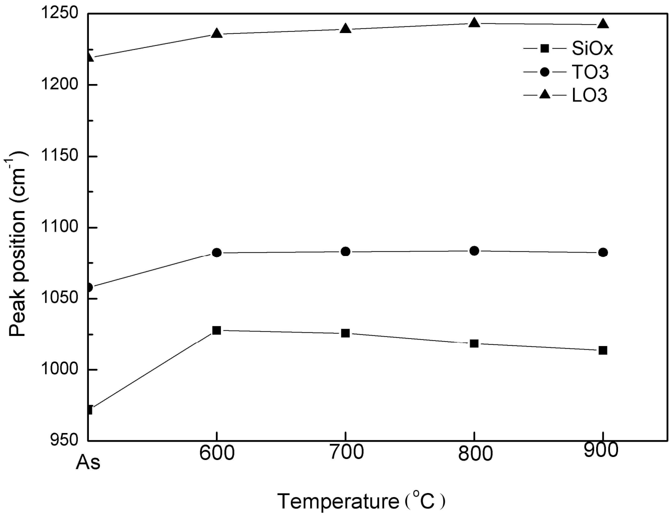

Fig. 3.15. The change in the peak positions with annealing for Ge-L4

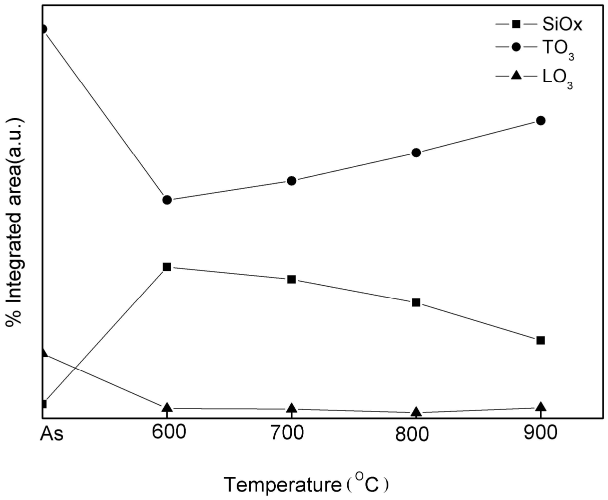

Fig. 3.16 The change in % integrated areas with annealing for Ge-L4

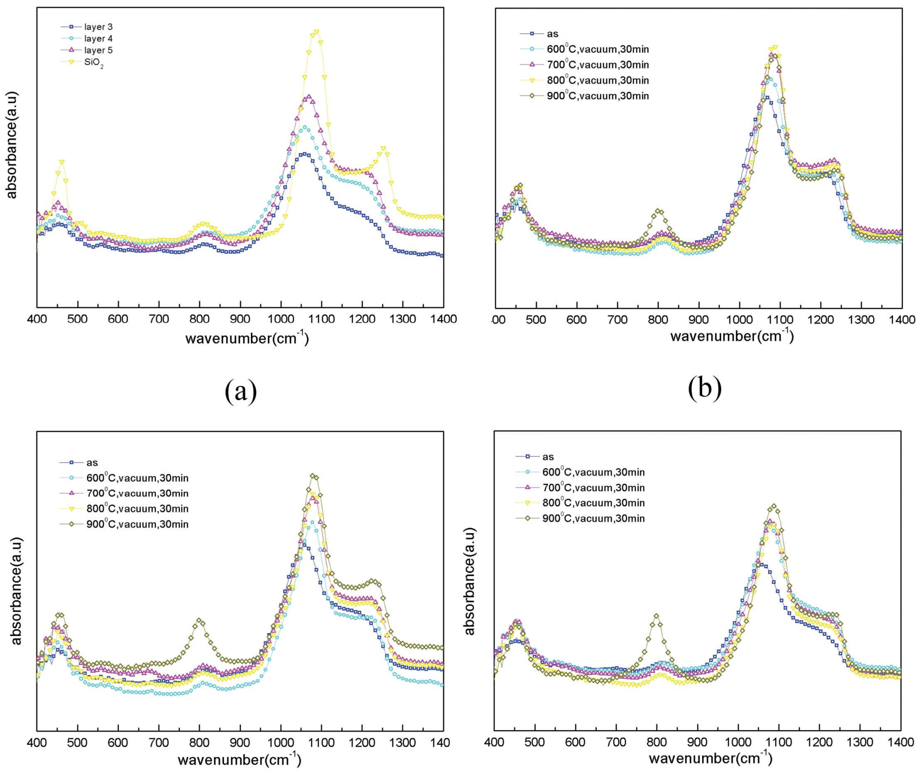

(a) (b)

(c) (d)

Fig. 3.17 FTIR spectra of (a) each layer and sputtered SiO_2, (b) Ge-L5, (c) Ge-L4 and (d) Ge-L3 with changing annealing temperature

FTIR spectra of each layer are plotted in Fig. 17, 18, 19 and 20. Variation of deconvolved SiO_x, TO_3 and LO_3 peak positions with respect to Ge concentration is plotted in Fig. 3.21. While the peak position of the TO_3 shift to lower wave number slightly, the SiO_x follows the same trend drastically with increasing Ge concentration. The reason could be the increase in elemental Ge concentration to GeO_x and GeO_2 at higher Ge concentrations due to decrease in SiO_2 contribution to co-sputtered film [62]. In spite of the strong Ge concentration dependence of the LO_3 absorption, variation in the TO_3 absorption is relatively small. LO_3 absorption intensity relative to TO_3 decreases with increasing germanium concentration [82].

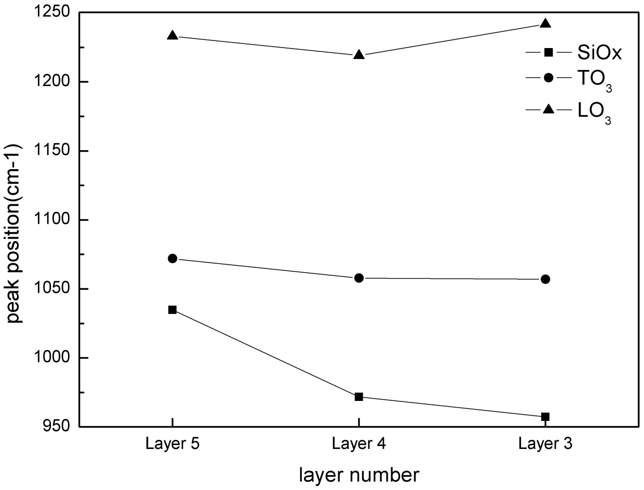

Fig. 3.18 Peak position dependence on Ge concentration for as samples

CHAPTER 4

SYNTHESIS AND CHARACTERIZATION OF SILICON NANOCRYSTALS

4.1. Sample Preparation

Two sets of multilayer sample were prepared; first set was deposited onto 40 nm thermally oxidized n-type Si substrate with (100) orientation and second onto 4 nm thermally oxidized n-type Si substrate with (100) orientation. Both were subjected to standard Si surface cleaning procedure and heated in the sputtering chamber at 500^{o}C for 30 minutes under vacuum in order to remove residual contamination and water molecules at the substrate surface. The base pressure of the chamber was 1.7x10^{-6} Torr before the depositions. Multilayer Si+SiO_2 thin films were deposited at room temperature by co-sputtering of 3 inch diameter Si (99.999% pure) and 3 inch diameter SiO_2 (99.995% pure) targets in Argon ambient using Vaksis nano-D 100 sputtering system. Si concentration of the layers was controlled with the magnitude of applied DC power to Si and RF power to SiO_2 targets. Thickness of the films was controlled with sputtering time. Sputtering pressure was fixed at 3 mTorr during the depositions. Multilayer samples, named as S1 and S2 (see Fig. 4.1 and 4.2) were prepared for Transmission Electron Microscopy (TEM) measurements. The details of the process parameters are listed in Table 4.1 and 4.2. S1 was prepared to understand roughly the Si concentration dependence of nanocrystal formation and to gain a view for future works. S2 was the detailed investigation of Si concentration between layer 3 and 4 of sample S1. Both Si and SiO_2 targets' power were doubled in deposition of S2 in order to get thicker films in a shorter time. Each layer of S2 was deposited on another set of substrates as shown in Fig. 4.3, for Photoluminescence (PL) spectroscopy. Samples were named as Si-L1, Si-L2, Si-L3, Si-L4 and Si-L5 referring to corresponding S2 layers.

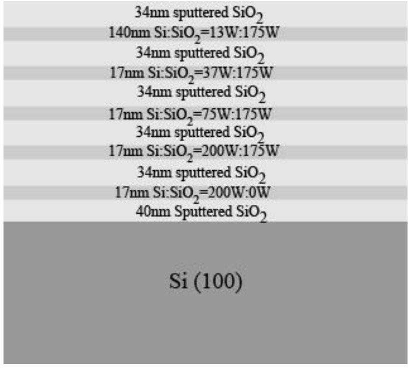

Fig. 4.1 Multilayer sample S1

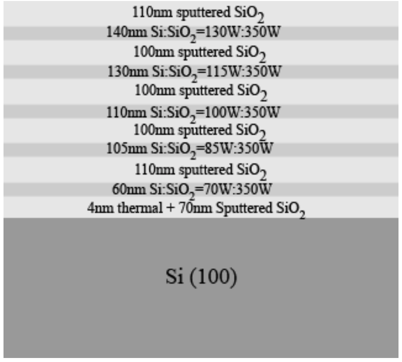

Fig. 4.2 Multilayer sample S2

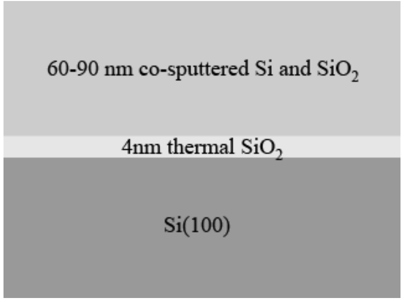

Fig. 4.3 Two layer sample Si-L series

Table 4.1 Sputtering conditions of multilayer sample S1

Layer #	Si target power (W)	SiO_2 target power (W)	Sputter time (min)
5	13	175	25
4	34	175	20
3	77	175	15
2	200	175	9
1	200	0	14

Table 4.2 Sputtering conditions of multilayer sample S2 and two layer Si-L series

Layer #	Two layer sample name	Si target power (W)	SiO_2 target power (W)	Sputter time (min)
5	Si-L5	130	350	75
4	Si-L4	115	350	75
3	Si-L3	100	350	75
2	Si-L2	85	350	75
1	Si-L1	70	350	60

Sample S1 was annealed at 900^{o}C, 1000^{o}C and 1050^{o}C for 1 hour and sample S2 at 1100^{o}C for 3 hours under N_2 atmosphere. Two layer samples were annealed at 900^{o}C, 1000^{o}C, 1050^{o}C and 1100^{o}C for 1 and 3 hours under N_2 atmosphere to form nanocrystals. Some of them were annealed at 500^{o}C for 20 min under H_2+N_2 to investigate effects of dangling bond passivation with hydrogen and others annealed at 900^{o}C for 10 min, 20 min and 90 min under O_2 to understand effects of oxidation on nanocrystals. All annealing processes were carried out in fused quartz furnace under N_2 environment.

4.2. Transmission Electron Microscopy

Various methods have been used to study nanocrystals, but TEM is the most powerful technique to measure nanocrystals' shape, size distribution, density and location in the matrix. On the other hand extremely careful sample preparation steps and high operation costs do not allow analysis of large number of samples.

4.2.1. Instrumentation

TEM measurements were carried out with 200 keV field emission analytical JEOL2010F. Cross sectional TEM specimens were prepared by standard procedure, i.e. each sample was cut into pieces with diamond saw then two of the pieces glued together with deposited layers facing each other next mechanically thinned and finally thinned down to electron transparency by ion milling.

4.2.2. Measurements and Discussion

4.2.2.1. Set 1

In the TEM image of as-sputtered sample (S1), excess Si precipitation was not detected in any layer (see Fig. 4.4). On the other hand, SAD confirms the crystallization in the 1050^{o}C annealed sample as can be seen from Fig. 4.5. Especially near the surface of the film there are various cracks and voids. Voids get larger with increasing annealing temperatures. Layer 1 crystallizes with annealing and forms polycrystalline continuous layer, as expected, see Fig. 4.4. Nanocrystal formation starts in the co-sputtered layers 2 and 3 with annealing at 1000^{o}C. The particle size is difficult to determine in layer 2 due to the density of the particles. Frequency distribution of layer 3 with annealing is shown in Fig. 4.7. The mean nanocrystal size is approximately 3 nm. Change of annealing temperature from 1000^{o}C to 1050^{o}C does not affect the mean nanocrystals size and size distribution. HRTEM image of a nanocrystal formed in this layer for 1050^{o}C is shown in Fig. 4.6. The nanocrystal oriented along (220) with a 2Å plane separation. Randomly scattered nanocrystals form about the upper half of the SiO_2 film in layers 4 and 5. The nanocrystals that formed near the layers 4 and 5 were in the order of 5 nm in size. In the case of low atomic concentration, Si atoms the diffuse to the interface and accumulate there due to the mobility difference. Accumulated Si atoms form nanocrystals in the interface layers. This effect is further investigated in the sample S2.

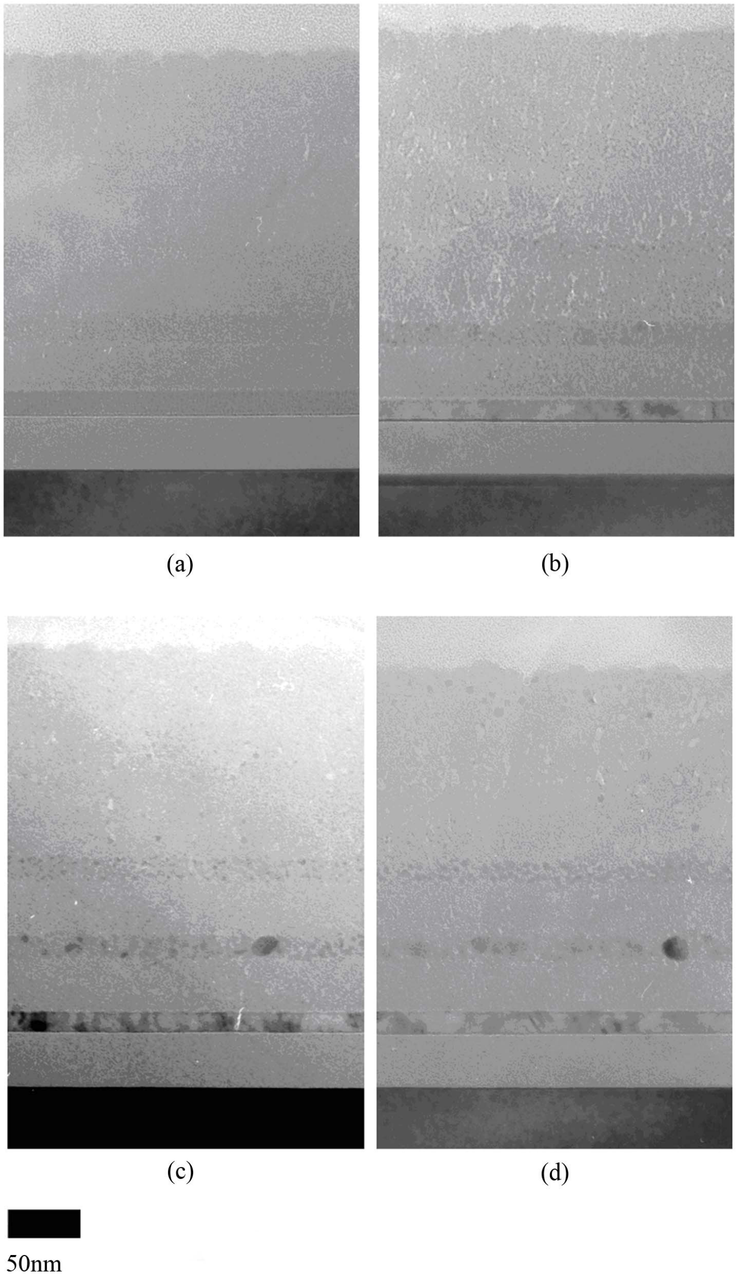

(a) (b)

(c) (d)

Fig. 4.4 TEM image of (a) as-sputtered, annealed at (b) 900°C, (c) 1000°C and (d) 1050°C samples

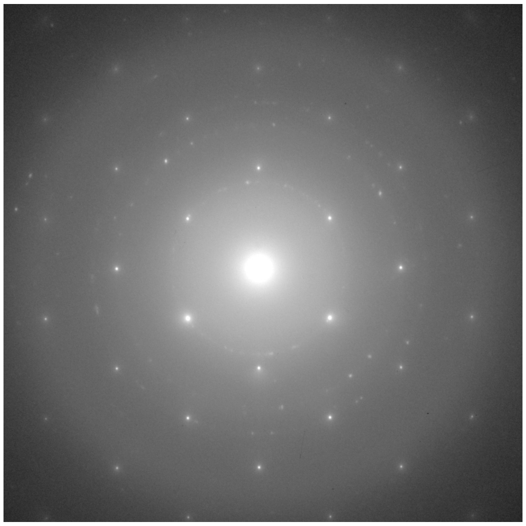

Fig. 4.5 SAD of the sample annealed 1050°C

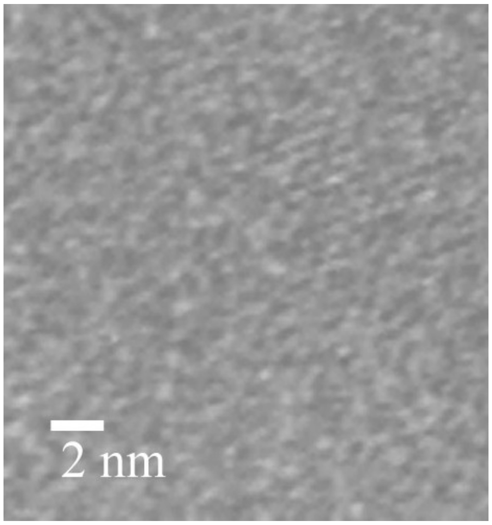

Fig. 4.6 HRTEM image of the nanocrystal in layer 3 annealed at 1050°C

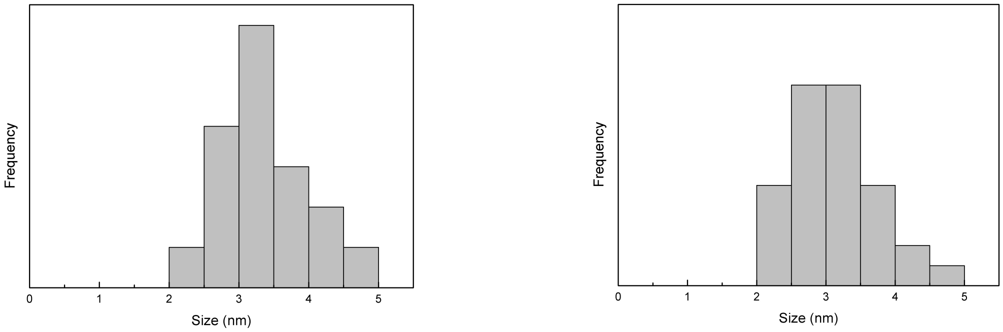

(a)

(b)

Fig. 4.7 Nanocrystal size distribution in layer 3 for annealing at 1000°C (a) and1050°C (b)

4.2.2.2. Set 2

In the TEM image of as sputtered S2 no single particle can be distinguished in any layer (see Fig. 4.8). On the other hand, high density of voids and cracks formed in the layers during sputtering. As can be seen from Fig. 4.9, these voids and cracks fairly disappeared after annealing at 1100°C for 3 hours.

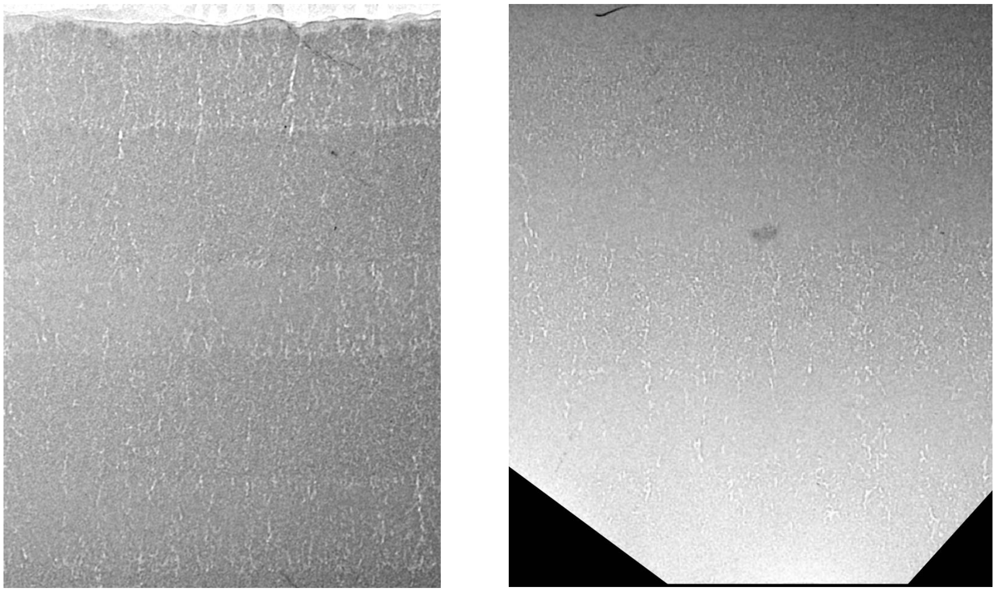

(a) (b)

Fig. 4.8 TEM images of upper (a) and lower (b) layers of as-sputtered sample

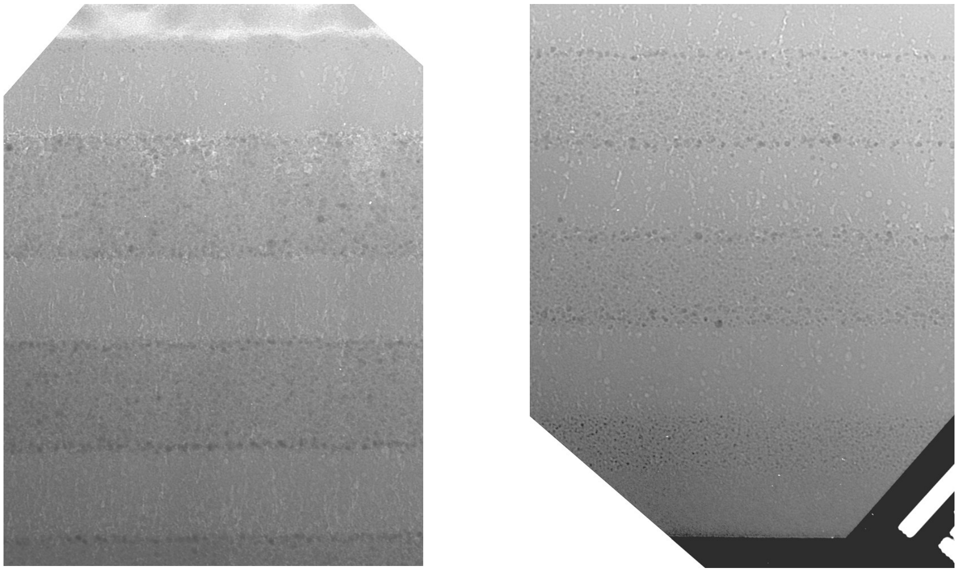

(a) (b)

Fig. 4.9 TEM images of upper (a) and lower (b) layers of annealed sample

TEM overview and detailed images of each layer are shown in Fig. 4.10 and 4.11, respectively. Deposition rate of Si increases with increasing target power and co-sputtered layer thickness increases from bottom to top for fixed deposition time. Particles do not show uniform distribution in the co-sputtered films. It is hard to measure size distribution of Si nanocrystals for each layer due to low contrast between Si and SiO_2 and high particle density. High Resolution Transmission Electron Microscopy (HRTEM) is necessary to measure particle size, which is cumbersome for this sample. Selected Area Diffraction (SAD) of the sample confirms the crystal formation with (111), (220) and (311) orientations (see Fig. 4.12). Co-sputtering of Si with SiO_2 deforms the oxide matrix hence the mobility of excess Si atoms in this layer is higher than sputtered SiO_2 alone. Low concentration of excess Si atoms degrades big nanocrystal formation inside the layers. Si atoms diffuse through the matrix and accumulate near the interfaces and form big nanocrystals. Increasing concentration of excess Si near the interfaces with accumulation results in ~15 nm Si nanocrystal band at interfaces. Nearly 2nm diameter nanocrystals spread through layer 2 and ~8 nm nanocrystals accumulated along the oxide interface. Increasing Si concentration in layer 3 and 4 enhances big nanocrystal growth inside these layers, hence average nanocrystals size increases at these samples. Interface nanocrystal density in layer 5 decreases profoundly with big nanocrystal formation inside the layer. There is not an abrupt difference in excess Si concentration in layer 1 and 2 but nanocrystals ~2 nm in size distribute through layer 1 homogenously. The reason could be the thickness of layer. Upper and lower Si nanocrystals form about 30 nm band in other layers which is comparable with the thickness of layer 1.

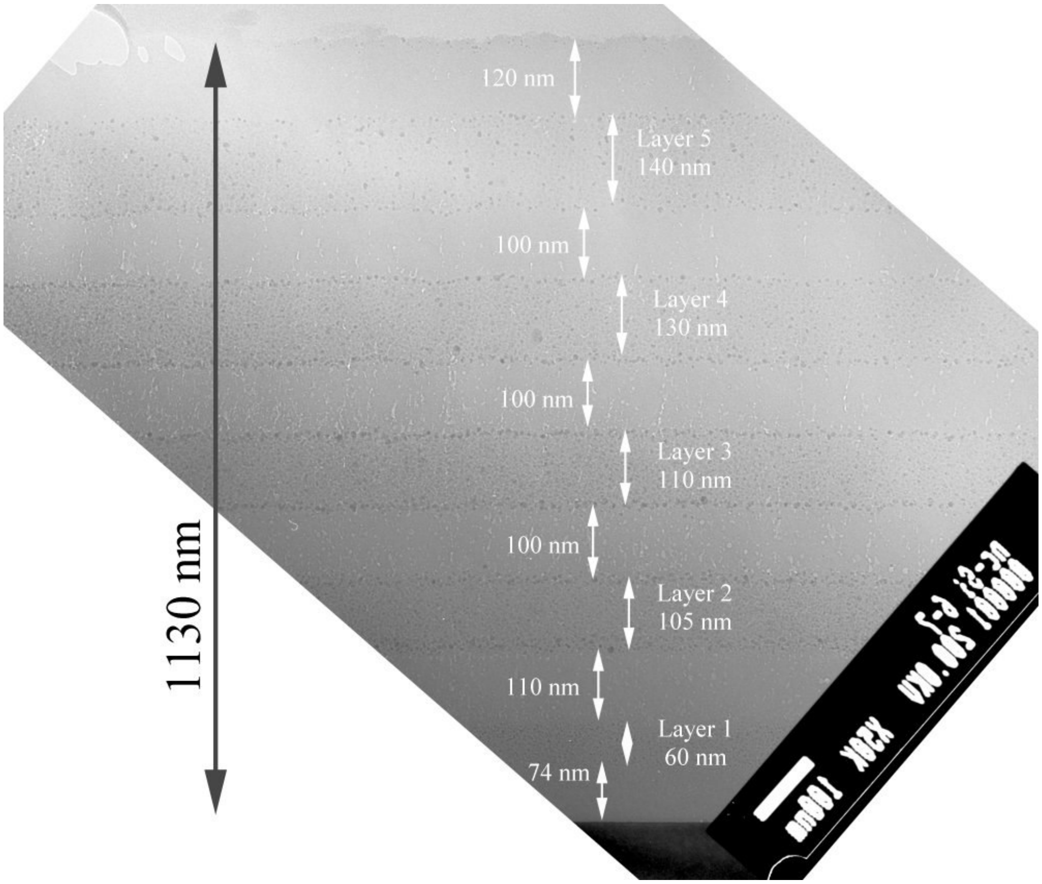

Fig. 4.10 TEM overview of multilayer sample

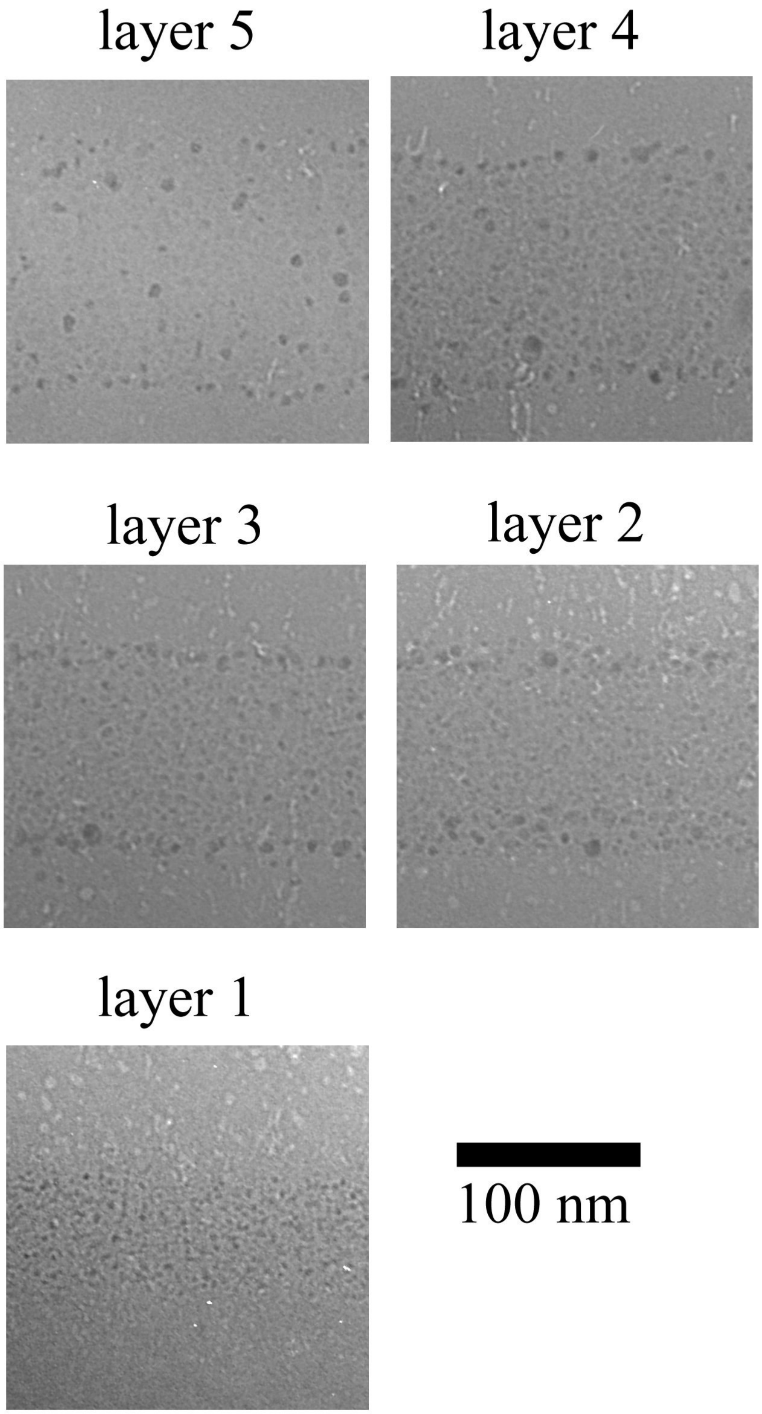

Fig. 4.11 Detailed TEM images of each layer

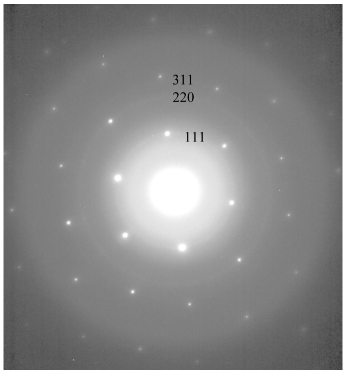

Fig. 4.12 SAD pattern of annealed S2

4.3. Photoluminescence Spectroscopy

Photoluminescence (PL) spectroscopy is a non-destructive, non-contact and effective technique to probe direct or quasi-direct band structure of nanocrystals. Many researches were carried out to understand size and band structures of Si nanocrystals with photo-excitation and recombination of electron-hole pairs inside the nanocrystals and surrounding interface [83-85].

4.3.1. Instrumentation

PL experiments were carried out at room temperature with an excitation source of 532 nm Nd:YAG laser (using a frequency doubler), MS-257 monochromator and Hamamatsu CCD camera.

4.3.2. Measurements and Discussion

Effect of annealing temperature and time on luminescence of Si nanocrystal are investigated. Samples annealed above 900°C show a broad Photoluminescence spectrum covering visible to near infrared, ~600 nm to 1000 nm, as shown in Fig. 4.13. PL peak shift to red linearly with increasing Si concentration indicates smooth increase in average nanocrystal size and quantum confinement effect on luminescence. As seen from Fig. 4.14, same trend is observed when the samples are annealed at 1000°C and 1050°C for 1 and 3 hours. Concentration of Si above Si-L3 annealing temperature does not play a critical role in nanocrystal size distribution.

Nanocrystal size distributions are not effected from annealing time as opposed to number of non-radiative defect centers which are affected fairly. PL intensity increases but PL peak does not shift with annealing time. López et. al. [86] suggest that "P_b centers are radiative recombination killers … long annealing treatments at high temperature in an inert atmosphere is a viable option". Luminescence is not only related to electron and hole recombination in Si nanocrystals [87, 88] but also Si/SiO_2 interface states [89]. Shimizu-Iwayama et. al. [90] suggests luminescence could also be related to interaction of neighboring nc-Si via a thin SiO_2 layer between the crystals, when nanocrystal population is very dense. Unfortunately, there is a disagreement in the literature on the origin of luminescence. In the present study integrated area of photoluminescence spectra is plotted for each sample for various annealing conditions in Fig. 4.15. Integrated area increases with increasing excess Si concentration up to Si-L3 and then decreases. It is likely that decrease in nanocrystal surface to volume ratio with increasing average nanocrystal size reduces the relative intensity of interface state luminescence.

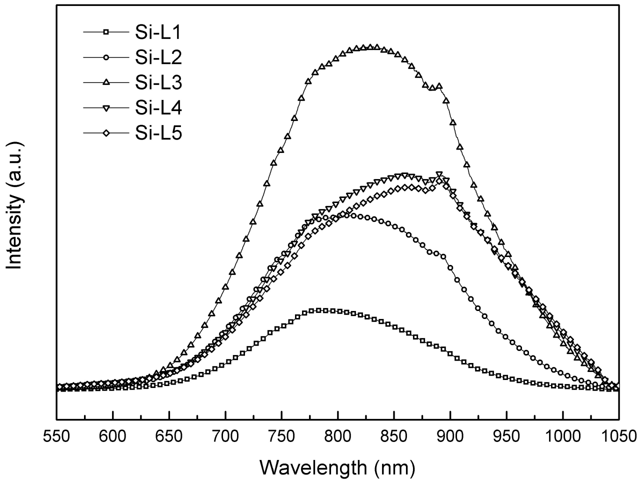

Fig. 4.13 PL spectra of each sample annealed at 1100°C, 3h, N_2

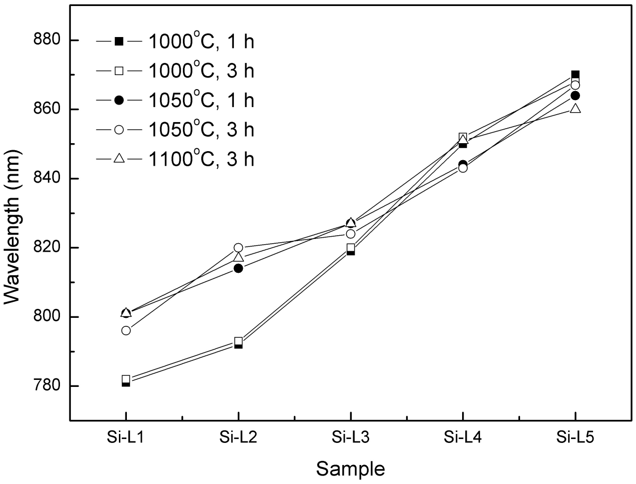

Fig. 4.14 PL spectra peak position dependence on annealing conditions

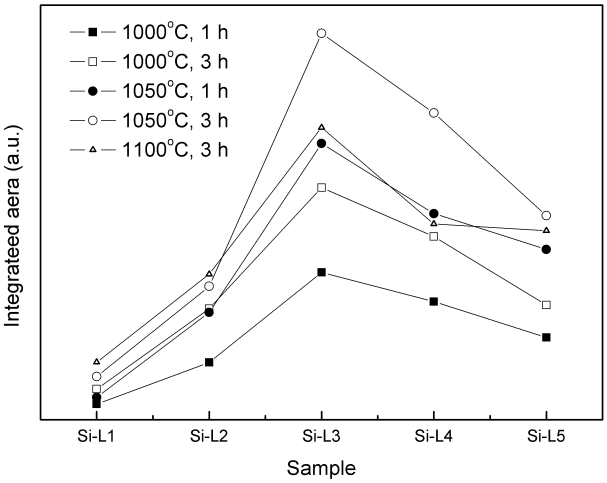

Fig. 4.15 PL spectra integrated area dependence on excess Si concentration

Hydrogen post annealing to passivate non-radiative defect centers either inside the Si nanocrystals or Si/SiO$_2$ interface is promising low cost thermal process to increase PL efficiency of Si nanocrystals. To investigate effects of dangling bond passivation, samples were annealed at 500°C for 20min under H_2+N_2. Increase in PL intensity and red shift in PL peak were observed (see Fig. 4.16). Wang et. al. [91] demonstrated that neither nanocrystal mean size nor density change with passivation at 500°C. To confirm the effects of passivation, samples were annealed at 750°C under N_2 for 30 min then spectrum turned back to its previous form with the release of hydrogen. Cheylan et. al. [92] state that "The fact that H passivation increases the emission intensity by up to an order of magnitude implies that only a small fraction of nanocrystals is defect free. Moreover, because the surface area and volume of crystallites increases rapidly with increasing size, it is reasonable to expect that larger crystallites will contain more nonradiative defects. This being the case, H passivation is expected to have a greater affect on the emission from larger nanocrystals than from smaller ones, giving rise to an apparent red shift in the composite spectrum". After hydrogen passivation steeper PL peak shift was observed with increasing Si concentration as shown in Fig. 4.17. This is reasonable since non-radiative defects are much probable in bigger nanocrystals. It is hard to determine the nanocrystal size distribution by PL measurements since non-radiative defects play an important role in the spectra. Cheylan et al. [93] states that "… correlations between a particle size distribution determined by techniques such as transmission electron microscopy, which favor larger nanocrystals, and PL emission spectra, which are dominated by smaller nanocrystals, could easily lead to erroneous conclusions. Even after passivation, it is unclear that the emission is representative of the full particle size distribution".

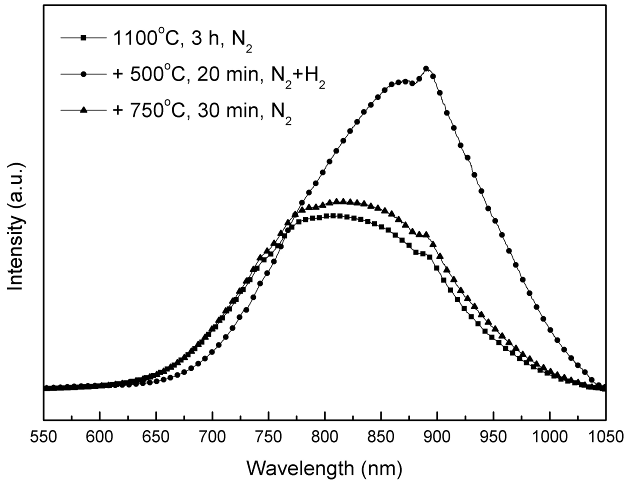

Fig. 4.16 Hydrogen post annealing effect on PL spectra for sample Si-L2

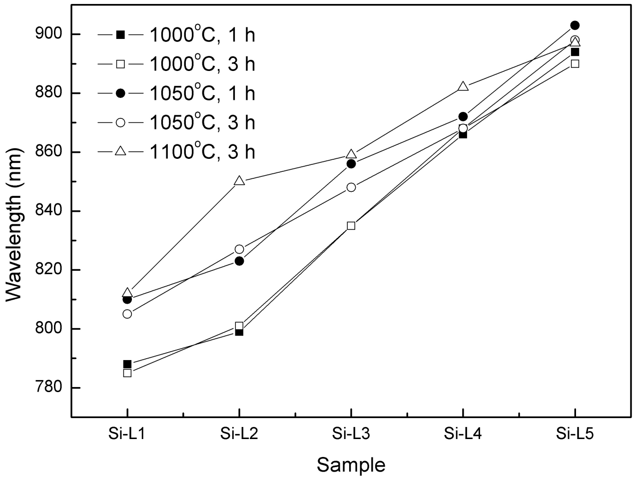

Fig. 4.17 PL spectra peak position after H_2 post annealing

Oxidation of Si nanocrystals is a technique to tune luminescence properties of crystals [94], passivation of oxygen deficiency P_b centers at Si/SiO_2 interface [95] and limit oxidation rates in other oxidizing conditions during device processing [96]. To investigate effects of oxidation, Si nanocrystals were formed by annealing at 1000°C for 3h under N_2 then annealed at 900°C for 10min, 20min and 90min under O_2. PL intensity decreases and spectrum shifts to blue with oxidation of nanocrystals as shown in Fig. 4.18. Blue shift in PL peak can be attributed to the decrease in average nanocrystal size with oxidation nanocrystals. Decrease in intensity is a result of decrease in density of nanocrystals [94]. PL peak shifts to blue linearly at short annealing time then slows down and stabilizes at higher annealing times (see Fig. 4.19). Scheer et. al. [96] and Coffin et. al. [97] observed the same effect and attributed this behaviour to a self-limiting oxidation of Si nanocrystals below the viscoelastic temperature of SiO_2 due to compressive stress normal to the SiO_2 /Si interface. Oxidation rate of Si decreases with increase in surrounding SiO_x shell and stress induced on Si core.

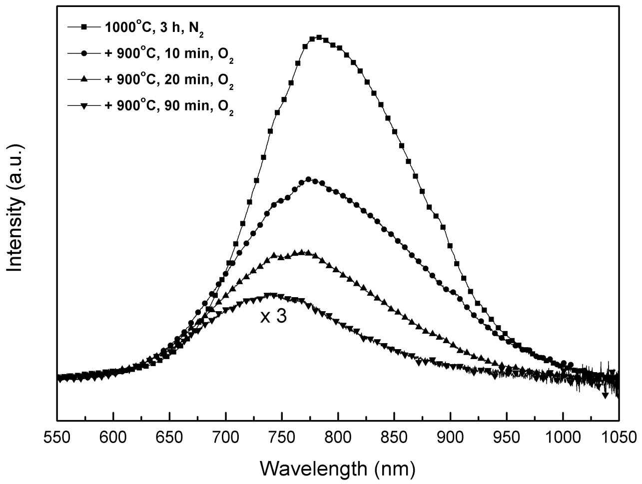

Fig. 4.18 Oxidation of Si nanocrystals in Si-L2 by annealing at 900°C for 10, 20 and 90 min under O_2

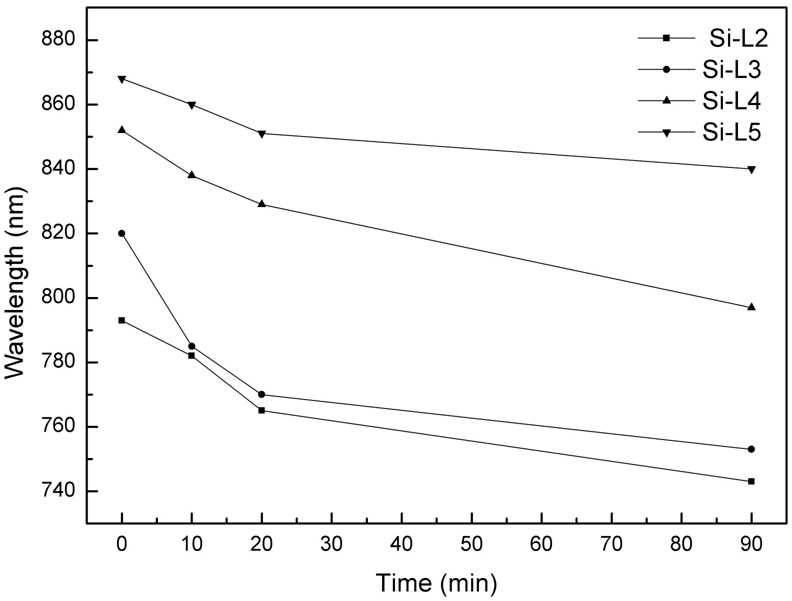

Fig. 4.19 PL peak shift with oxidation of Si nanocrystals for various Si concentration

CHAPTER 5

CONCLUSION

In this study, Ge and Si containing multi and single layer SiO_2 films were deposited on Si substrates at various concentrations by magnetron sputtering deposition technique and then nanocrystals were formed with high temperature thermal annealing in quartz furnace. Effects of annealing temperature and time on Ge and Si nanocrystal formation and effect of post annealing under hydrogen and oxygen on luminescence properties of Si nanocrystals were examined. Samples were analyzed by transmission electron microscopy, selected area diffraction, Raman, Fourier transform infrared and photoluminescence spectroscopy techniques.

It was shown that atomic Ge concentration and annealing temperature are the critical parameters for nanocrystal formation, size distribution, density, the stress induced by SiO_2 matrix and SiO_2 recovery. TEM images demonstrated that nanocrystal size strongly depend on Ge concentration in SiO_2. Nanocrystal diameters exceeding layer thickness can be formed at high Ge concentration. These nanocrystals deformed probably due to the nonuniform compressive stress induced by surrounding SiO_2. Well separated spherical nanocrystals can be observed at moderate Ge concentration. Nanocrystal size is fairly controllable with annealing temperature at moderate Ge concentration. Small Ge clusters were formed instead of nanocrystals at low Ge concentration. Ge nanocrystal mean radius increases with increasing annealing temperature as a result of increase in mobility of Ge atoms in SiO_2 matrix. There exist diffusion barrier effect of SiO_2 layers and this intern has a role in the nanocrystals' size. Raman spectroscopy confirmed the TEM results that high oxide stress induced on Ge nanocrystals with increasing nanocrystal size. Stress effect dominates in Ge-Ge traverse optical peak position competition with the phonon confinement effect. We also verified that there is recovery of oxide with nanocrystal formation.

Si concentration and diffusivity in oxide are the critical parameter for nanocrystal formation, size distribution, density and luminescence characteristic. TEM images demonstrated that Si nanocrystal size depend on local Si concentration in SiO_2. High density of voids and cracks formed in the as-sputtered sample mostly disappear after annealing. Low concentration of excess Si atoms in SiO_2 degrades big nanocrystal formation inside the layers. Big nanocrystal forms with the Si diffusion through the matrix and accumulation to interfaces. The density of big nanocrystals in interface decreases with increasing excess Si concentration. PL peak shifts to red linearly with increasing average nanocrystal size and intensity decreases with decreasing density of nanocrystals. Hydrogen post annealing enhances PL intensity and this in turn causes red shift of PL peak due to passivation of non-radiative P_b centers especially at big nanocrystals. PL peak shifts linearly with increasing average nanocrystal size for passivated samples. Si nanocrystals oxidized to tune luminescence spectra of nanocrystals. PL peak shifts to blue with a decrease in intensity indicating decrease in nanocrystal average size and density. Linear blue shift at short annealing time then slows down and stabilizes at higher annealing times attributed to the decrease in oxidation rate of Si nanocrystals with increase in surrounding SiO_x shell and stress induced on Si core.

REFERENCES

[1] J. V. McCanny and J. C. White. *VLSI Technology and Design*. Academic Press, 1987.

[2] G.E. Moore; *Electronics **38** 114 (1965)*

[3] Intel cooperation, *Moore's Law*, *http://www.intel.com/technology/mooreslaw/index.htm, 07/30/07*

[4] M. Law, J. Goldberger and P. Yang; *Annual Review of Material Research **34** 83 (2004)*

[5] P. Avouris, J. Appenzeller, R. Martel and S. J. Wind; *Proceedings of the IEEE **91** 1772 (2003)*

[6] R. A. Rao, R. F. Steimle, M. Sadd, C. T. Swift, B. Hradsky, S. Straub, T. Merchant, M. Stoker, S. G. H. Anderson, M. Rossow, J. Yater, B. Acred, K. Harber, E. J. Prinz, B. E. White Jr. and R. Muralidhar; *Solid-State Electronics **48** 1463 (2004)*

[7] H. Takagi, H. Ogawa, Y. Yamazaki, A. Ishizaki and T. Nakagiri; *Applied Physics Letters **56** 2379 (1990)*

[8] Intel cooperation, *What is a FLASH Memory*, *http://www.intel.com/design/flash/articles/what.htm#top, 07/30/07*

[9] M. She and T. J. King; *IEEE Transactions on Electron Devices **50** 1934(2003)*

[10] H. I. Hanafi, S. Tiwari and I. Khan; *IEEE Transactions on Electron Devices **43** 1553 (1996)*

[11] V. Beyera, J. von Borany and M. Klimenkov; *Journal of Applied Physics **101** 094507 (2007)*

[12] L. Pavesi, L. Dal Negro, C. Mazzoleni, G. Franzo and F. Priolo; *Nature **408** 440 (2000)*

[13] R.J. Walters, G. I. Bourianoff and H. A. Atwater; *Nature Materials **4** 143 (2005)*

[14] J. Heitmann, F. Müller, M. Zacharias and U. Gösele; *Advanced Materials **17** 795 (2005)*

[15] M. Kulakci, U. Serincan and R. Turan; *Semiconductor Science and Technology* ***21*** *1527 (2006)*

[16] E. S. Marstein, A. E. Gunnæs, U. Serincan, S. Jørgensen, A. Olsen, R. Turan and T. G. Finstad; *Nuclear Instruments and Methods in Physics Research B* ***207*** *424 (2003)*

[17] U. Serincan, G. Aygun and R. Turan; *Journal of Luminescence* ***113*** *229 (2005)*

[18] D. Comedi, O. H. Y. Zalloum, E. A. Irving, J. Wojcik, T. Roschuk, M. J. Flynn, and P. Mascher; *Journal of Applied Physics* ***99*** *23518 (2006)*

[19] S. Ağan, A. Çelik-Aktas, J. M. Zuo, A. Dana, A. Aydınlı; *Applied Physics A Materials Science & Processing* ***83*** *107 (2006)*

[20] D. Riabinina, C. Durand, M. Chaker, and F. Rosei; *Applied Physics Letter* ***88*** *073105 (2006)*

[21] P. M. Fauchet, J. Ruan, H. Chen, L. Pavesi, L. Dal Negro, M. Cazzaneli, R. G. Elliman, N. Smith, M. Samoc, and B. Luther-Davies; *Optical Materials* ***27*** *745 (2005)*

[22] H. G. Chew, W. K.Choi, Y. L. Foo, F. Zheng, W. K. Chim, Z. J. Voon, K. C. Seow, E. A. Fitzgerald and D. M. Y. Lai; *Nanotechnology* ***17*** *1964 (2006)*

[23] C. Bonafos, B. Colombeau, A. Altibelli, M. Carrada, G. B. Assayag, B. Garrido, M. López, A. Pérez-Rodríguez, J. R. Morante and A. Claverie; *Nuclear Instruments and Methods in Physics Research B* ***178*** *17 (2001)*

[24] Y. Maeda; *Physical Review B* ***51*** *1658 (1995)*

[25] W. K. Choi, V. Ng, S. P. Ng, H. H. Thio, Z. X. Shen and W. S. Li; *Journal of Applied Physics* ***86*** *1398 (1999)*

[26] J. D. Verhoeven. *Fundamentals of Physical Metallurgy.* John Wiley and Sons, 1975.

[27] I. M. Lifshitz and V. V. Slyozov*; Journal of Physics and Chemistry of Solids* ***19*** *35 (1961)*

[28] C . Wagner, *Z. Elektrochem.* ***65*** *581 (1961)*

[29] J. C. Cahn. *The Mechanism of Phase Transformations in Crystalline Solids, Fundamentals of Physical Metallurgy.* Institute of Metals: London (1969)

[30] M. Yamamoto, T. Koshikawa, T. Yasue, H. Harima and K. Kajiyama; *Thin*

Solid Films ***369*** *100 (2000)*

[31] TFT-LCD Research Center at Kyung Hee Univversity, *PECVD system*, http://tftlcd.khu.ac.kr/research/poly-Si/chapter4.html

[32] X. Y. Chen, Y. F. Lu, Y. H. Wu, B. J. Cho, M. H. Liu, D. Y. Dai, and W. D. Song; *Journal of Applied Physics* ***93*** *6311 (2003)*

[33] H. Seifarth, R. Grötzschel, A. Markwitz, W. Matz, P. Nitzsche and L. Rebohle; *Thin Solid Films* ***330*** *202 (1998)*

[34] J. L. Vossen and W. Kern. *Thin film processes.* Academic Press, 1978

[35] S. Hofmann; *Surface and Interface Analysis* ***30*** *228 (2000)*

[36] L. V. Vaeck, A. Adriaens and R. Gijbels; *Mass Spectrometry Reviews,* ***18*** *1 (1999)*

[37] O. M. N. D. Teodoro and A. M. C. Moutinho; *Nuclear Instruments and Methods in Physics Research B* ***222*** *609 (2004)*

[38] S. Oswald and S. Baunack; *Thin Solid Films* ***425*** *9 (2003)*

[39] S. Hofmann; *Philosophical Transactions: Mathematical, Physical & Engineering Sciences* ***362*** *55 (2004)*

[40] S. Hofmann; *Reports on Progress in Physics* ***61*** *827 (1998)*

[41] I. Berbezier, A. Karmous, A. Ronda, T. Stoica, L. Vescan, R. Geurt, A. Olzierski, E. Tsoi and A. G. Nassiopoulou; *Journal of Physics: Conference Series* ***10*** *73 (2005)*

[42] I. Berbeziera, A. Karmousa, P. D. Szkutnika, A. Rondaa, A. Sgarlatab, A. Balzarottib, P. Castruccib, M. Scarsellib and M. De Crescenzib; *Materials Science in Semiconductor Processing* ***9*** *812 (2006)*

[43] J. H. Comfort, L. M. Garverick and R. Reif; *Journal of Applied Physics* ***62*** *3388 (1987)*

[44] M. Sporn, G. Libiseller, T. Neidhart, M. Schmid, F. Aumayr, HP. Winter and P. Varga; *Physical Review Letters* ***79*** *945 (1997)*

[45] R. K. Waits; *Journal of Vacuum Science & Technology A: Vacuum, Surfaces, and Films* ***18*** *1736 (2000)*

[46] N. Matsunami, Y. Yamamura, Y. Itikawa, N. Itoh, Y. Kazumata, S. Miyagawa, K. Morita, R. Shimizu, and H. Tawara; *Atomic Data and Nuclear Data Tables* ***31*** *1 (1984)*

[47] J. E. Mahan, A. Vantomme; *Physical Review B* ***61*** *8516 (2000)*

[48] J. E. Mahan. *Physical Vapor Deposition of Thin Films.* Wiley, 2000

[49] H. E. Roosendaal. *Sputtering by Particle Bombardment Vol. I* Springer-Verlag, 1983

[50] J. J. Elich, H. E. Roosendaal and D. Onderlinden; *Radiation Effects and Defects in Solids* ***14*** *93 (1972)*

[51] O. Almen, G. Bruce; *Nuclear Instruments and Methods* ***11*** *279 (1961)*

[52] O. Almen, G. Bruce; *Nuclear Instruments and Methods* ***11*** *257 (1961)*

[53] R. V. Stuart and G. K. Wehner; *Journal of Applied Physics* ***33*** *2345 (1962)*

[54] D. E Harrison, G. D. Magnuson; *Physical Review* ***122*** *1421 (1961)*

[55] P. Sigmund; *Physical Review* ***184*** *2 384 (1969)*

[56] G. K. Wehner; *Journal of Applied Physics* ***10*** *159 (1968)*

[57] V. S. Smentkowski; *Progress in Surface Science* ***64*** *58 (2000)*

[58] P. Glöersen; *Journal of Vacuum Science and Technology* ***12*** *28, (1975)*

[59] K.B. Sundaram and A. Khan; *Thin Solid Films* ***295*** *87 (1997)*

[60] A. V. Kolobov, S. Q. Wei, W. S. Yan, H. Oyanagi, Y. Maeda and K. Tanaka; *Physical Review B* ***67*** *195314 (2003)*

[61] W. K. Choi, V. Ng., S. P. Ng, H. H. Thio, Z. X. Shen and W. S. Li; *Journal of Applied Physics* ***86*** *1398 (1999)*

[62] V. Ho, W. K. Choi, W. K. Chim, M. S. Tay, D. A. Antoniadis, E. A. Fitzgerald, A. Y. Du, C. H. Tung, R. Liu and A. T. S. Wee; *Applied Physics Letters* ***83*** *3558 (2003)*

[63] L. W. Teo, W. K. Choi, W. K. Chim, , V. Ho, C. M. Moey, M. S. Tay, C. L. Heng, Y. Lei, D. A. Antoniadis and E. A. Fitzgerald; *Applied Physics Letters* ***81*** *3639 (2002)*

[64] M. She, T. J. King, *IEEE Transactions on Electron Devices* ***50*** *1934 (2003)*

[65] W. K. Choi, V. Ho, V. Ng, Y. W. Ho, S. P. Ng, and W. K. Chim; *Applied Physics Letter* ***86*** *143114 (2005)*

[66] W. K. Choi, W. K. Chim, C. L. Heng, L. W. Teo, V. Ho, V. Ng, D. A. Antoniadis and E. A. Fitzgerald; *Applied Physics Letters* ***80*** *2014 (2002)*

[67] H. G. Chew, W. K. Choi, Y. L. Foo, F. Zheng, W. K.Chim, Z. J. Voon, K. C. Seow, E. A. Fitzgerald and D. M. Y. Lai; *Nanotechnology* ***17*** *1964 (2006)*

[68] A. Wellner, V. Paillard, C. Bonafos, H. Coffin, and A. Claverie, B. Schmidt and K.H. Heinig; *Journal of Applied Physics* ***94*** *5639 (2003)*

[69] U. Serincan, G. Kartopu, A. Guennes, T. G. Finstad, R. Turan, Y. Ekinci and S. C. Bayliss; *Semiconductor Science and Technology **19** 247 (2004)*

[70] A. V. Kolobov; *Journal of Applied Physics **87** 2926 (2000)*

[71] C. E. Bottani, C. Mantini, P. Milania, M. Manfredini, A. Stella, P. Tognini, P. Cheyssac and R. Kofman; *Applied Physics Letters **69** 2409 (1996)*

[72] M. Fujii, S. Hayashi and K. Yamamoto; *Japanese Journal of Applied Physics **30** 687 (1991)*

[73] W.K. Choi, H.G. Chew, F. Zheng, W. K. Chim, Y. L. Foo and E. A. Fitzgerald; *Applied Physics Letters **89** 113126 (2006)*

[74] I. D. Sharp, D. O. Yi , Q. Xu, C. Y. Liao, J. W. Beeman, Z. Liliental-Weber, K. M. Yu, D. N. Zakharov, J. W. Age,D. C. Chrzan and E. E. Haller; *Applied Physics Letters **86** 063107 (2005)*

[75] P. Lange; *Journal of Applied Physics **66** 201 (1989)*

[76] D. W. Berreman; *Physical Review **130** 2193 (1963)*

[77] C. T. Kirk; *Physical Review B **38** 1255 (1988)*

[78] M. Modreanua, M. Gartnerb, E. Aperathitisc, N. Tomozeiud, M. Androulidakic, D. Cristeae and P. Hurleya; *Physica E **16** 461 (2003)*

[79] W. K. Choi, Y. W. Ho, S. P. Ng, and V. Ng; *Journal of Applied Physics **89** 2168 (2001)*

[80] U. Serincan, S. Yerci, M. Kulakci and R. Turan; *Nuclear Instruments and Methods in Physics Research B **239** 419 (2005)*

[81] C. G. Ahn and H. S. Kang; *Journal of Applied Physics **86** 1542 (1999)*

[82] M. Fujii, M. Wada, S. Hayashi and K. Yamamato; *Physical Review B **46** 15930 (1992)*

[83] M. L. Brongersma, A. Polman, K. S. Min, E. Boer, T. Tambo, and H. A. Atwater; *Applied Physics Letters **72** 2577 (1998)*

[84] M. L. Brongersma, P. G. Kik, A. Polman, K. S. Min and H. A. Atwater; *Applied Physics Letters **76** 351 (2000)*

[85] J. Heitmann, F. Müller, L. Yi, M. Zacharias, D. Kovalev and F. Eichhorn; *Physical Review B **69** 195309 (2004)*

[86] M. López, B. Garrido, C. García, P. Pellegrino, A. Pérez-Rodríguez, J. R. Morante, C. Bonafos, M. Carrada, and A. Claverie; *Applied Physics Letter **80** 1637 (2002)*

[87] T. Takagara and K. Takeda; *Physical Review B* ***46*** *15578 (1992)*

[88] V. Ranjan; V. A. Singh and G. C. John; *Physical Review B* ***58*** *1158 (1998)*

[89] Y. Kanemitsu, T. Ogawa, K. Shiraishi and K. Takeda; *Physical Review B* ***48*** *4883 (1993)*

[90] T. Shimizu-Iwayama, D. E. Hole and I. W. Boyd; *Journal of Physics: Condensed Matter* ***11*** *6595 (1999)*

[91] Y. Q. Wang, R. Smirani and G. G. Ross; *Physica E* ***23*** *97 (2004)*

[92] S. Cheylan and R. G. Elliman; *Applied Physics Letters* ***78*** *1225 (2001)*

[93] S. Cheylan and R. G. Elliman; *Applied Physics Letters* ***78*** *1912 (2001)*

[94] M. L. Brongersma, A. Polman, K. S. Min, E. Boer, T. Tambo, and H. A. Atwater; *Applied Physics Letters* ***72*** *2578 (1998)*

[95] L. Bi, Y. He and J.Y. Feng; *Journal of Crystal Growth* ***289*** *564 (2006)*

[96] K. C. Scheer, R. A. Rao, R. Muralidhar, S. Bagchi, J. Conner, L. Lozano, C. Perez, M. Sadd, and B. E. White, Jr.; *Journal of Applied Physics* ***93*** *5637 (2003)*

[97] H. Coffin, C. Bonafos, S. Schamm, N. Cherkashin, G. Ben Assayag, A. Claverie, M. Respaud, P. Dimitrakis and P. Normand; *Journal of Applied Physics* ***99*** *044302 (2006)*